Direct Measurement of Boiling Water Heat Flux for Predicting and Controlling Near Critical Heat Flux

Jordan L. Thompson

Thesis submitted to the faculty of the Virginia Polytechnic Institute and State University
in partial fulfillment of the requirements for the degree of

Master of Science
In
Mechanical Engineering

Alan A. Kornhauser, Chair
Thomas E. Diller
Scott T. Huxtable

May 8, 2013
Blacksburg, VA

Keywords: heat flux sensor, boiling, critical heat flux

Direct Measurement of Boiling Water Heat Flux for Predicting and Controlling Near Critical Heat Flux

Jordan L. Thompson

ABSTRACT

A novel method for measuring heat flux of boiling water is designed and built to study critical heat flux (CHF) and observe the response of a heat flux sensor when CHF occurs. A high temperature heat flux sensor is embedded in the wall of a pipe to get a direct measurement of the surface heat flux and sensor temperature. By submerging the pipe in water and applying a controlled heat flux to the inside diameter over the area where the sensor is located, boiling is created on the outer surface while measuring the heat flux. The heat flux is gradually increased up to CHF and the heat flux response is observed to determine if the heat flux sensor could sense CHF when it occurred. The heat flux sensor is able to consistently measure the value for CHF, which is approximately 510 kW/m² for this system. It is also observed during the experiments that the heat flux response undergoes an inflection of the heat transfer coefficient at a consistent temperature just before reaching CHF. This observed inflection caused the heat flux response to deviate from its cubic relationship with the temperature and drastically increase for a very small change in temperature. This inflection response can be used as an indication for approaching CHF and can also be used to approximate its value without prior knowledge of when it occurs.

Table of Contents

List of Figures

List of Tables

Nomenclature

A	area (m²)
C	critical heat flux proportionality constant
C_p	specific heat (kJ/kg·K)
$C_{s,f}$	surface-fluid coefficient
D	diameter (in)
Gr_L	Grashof number
I	current (A)
K	natural convection constant
L	length (in)
Nu_L	Nusselt number
P	Power (W)
Pr	Prandtl number
R	resistance (Ω)
$R"$	thermal resistance (m²K/W)
Ra_L	Rayleigh number
S	sensor sensitivity (μV/(W/cm²))
T	temperature (°C)
U	expanded uncertainty
$\mathcal{V}$	volume (m³)
V	voltage (V)
V_{out}	sensor output voltage (μV)
c	surface heat flux proportionality constant (W/m²·K³)
g	gravitational acceleration (m/s²)
h	heat transfer coefficient (W/m²·K)
h_{fg}	enthalpy of vaporization (kJ/kg)
k	thermal conductivity (W/m·K)
m	natural convection exponent
n	surface-liquid combination exponent
q	heat transfer rate (W)
$q"$	heat flux (W/m²)
r	electrical resistivity (Ω m)
t	time (s)
u	standard uncertainty

Greek Letters

α	temperature coefficient of resistance (1/°C)
β	coefficient of thermal expansion (1/K)
δ	thickness (m)
ε	emissivity
θ	dynamic receding contact angle (°)
μ	viscosity (N·s/m²)
ν	kinematic viscosity (m²/s)
ρ	density (kg/m³)
σ	surface tension (N/m)
σ_{SB}	Stefan-Boltzman constant (5.67×10^{-11} kW/m^2·K^4)
ϕ	surface orientation angle (°)

Subscripts

abs	absorbed
avg	average
b	boiling
c	cross sectional
$cond$	conduction
$conv$	convection
$diff$	differential
e	excess
$heater$	pertaining to the face of the heater
in	input
inc	incident
l	liquid
max	maximum
out	output
rr	re-radiation
s	surface
sat	saturation
$slug$	pertaining to heat flux from slug calorimeter method
tot	total
v	vapor
var	variable transformer
w	pertaining to the wall between the sensor and surface
0	initial/room temperature
∞	bulk fluid

1 Introduction

Boiling heat transfer gives very high heat fluxes for small temperature differences, and is thus an efficient way to transfer thermal energy. Systems that employ boiling heat transfer, such as nuclear reactors, are designed to operate in the nucleate boiling regime. The critical heat flux (CHF) represents the maximum heat flux that can be achieved in the nucleate boiling regime, and for systems with a constant heat flux boundary condition CHF is the limit of safe operation for that system. Once CHF is exceeded with a constant heat flux boundary condition, film boiling blankets the surface with a layer of vapor and causes the surface temperature to quickly rise to extreme levels, often destroying the system. This is especially important for nuclear reactors because if CHF is reached meltdown occurs, which can cause contamination of the cooling water and radiation release.

Due to the complex nature of boiling, theoretical models are difficult to generate and correlations for nucleate boiling and CHF are often determined experimentally. Many experiments have been done to determine when CHF occurs for various conditions and configurations but the results only apply to those conditions and configurations. By using a heat flux sensor to control a controlled heater, heat flux can be maintained at CHF levels without exceeding CHF and causing burnout. This allows in-situ measurements of CHF in the experimental apparatus and operating equipment. Such measurements could allow systems using boiling heat transfer to safely operate closer to CHF, possibly improving performance. One possible application these types of measurements are in nuclear fuel rods where burnout causes serious problems. Future research may result in using this in-situ measurement method for preventative meltdown purposes.

2 Background

The different regimes of pool boiling heat transfer were first observed by Nukiyama [1]. By using an electrically heated nichrome wire submerged in water, he found that when increasing the power the heat flux increased quickly for small increases in excess temperature, the difference between surface temperature and saturation temperature, until at a specific heat flux the temperature of the wire jumped to the melting point and the wire burned out. This heat flux was identified from this experiment as the maximum heat flux that can be achieved during nucleate boiling, which was named the critical heat flux (CHF). Nukiyama was able to surpass CHF by using a platinum wire, which has a higher melting point, and was able to develop most of the boiling curve shown in Figure 1. This sudden increase in temperature occurs because a constant heat flux boundary condition is created by controlling the power input. The constant heat flux boundary condition prevents the heat flux from decreasing after CHF occurs. Nukiyama speculated that if the temperature could be controlled rather than the power then this sudden temperature increase would not occur. Drew and Mueller [2] were able to confirm Nukiyama's theory and observe the portion of the boiling curve between the maximum and minimum heat flux by boiling organic compounds while using saturated steam to create a constant temperature boundary condition.

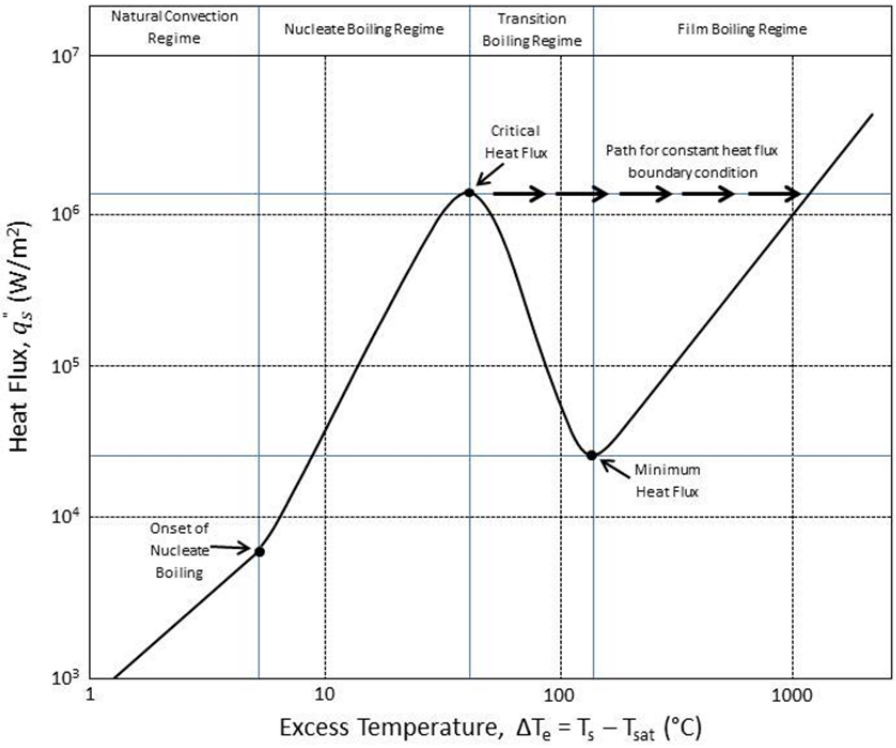

Figure 1. Boiling curve for pool boiling determined by Nukiyama.

The first, successful heat flux correlation for the nucleate boiling regime was developed by Rohsenow [3] and is still commonly used today. The Rohsenow correlation for nucleate boiling heat flux is

$$q"_s = \mu_l h_{fg} \left[\frac{g(\rho_l - \rho_v)}{\sigma}\right]^{1/2} \left(\frac{C_{p,l}\,\Delta T_e}{C_{s,f}\,h_{fg}\,Pr_l^n}\right)^3 \tag{1}$$

where the excess temperature is equal to

$$\Delta T_e = T_s - T_{sat} \tag{2}$$

The surface coefficient $C_{s,f}$ and exponent n are introduced to account for different solid-liquid combinations and are found experimentally. Values for $C_{s,f}$ and n are reported by Pioro [7] and by Incropera and Dewitt [9].

In order to predict when CHF occurs for a specific system, a correlation for CHF was developed by Kutateladze [4] and Zuber [5];

$$q"_{max} = C\,h_{fg}\,\rho_v^{1/2}\,[\sigma\,g(\rho_l - \rho_v)]^{1/4} \tag{3}$$

Unlike the Rohsenhow correlation from Equation (1), the correlation for CHF in Equation (3) is not dependent on surface material and is instead dependent on surface geometry through the CHF constant C. Zuber reports that a value for C of $\pi/24$, or about 0.131, applicable to large horizontal cylinders, spheres, and many other large finite surfaces. Chang [13], as referenced by Kandlikar [11], states that C is equal to 0.098 for vertical surfaces. The Kutateladze-Zuber correlation from Equation (3) is the generally accepted correlation for CHF. However, it is accurate only if C is known for a specific configuration. Kandlikar [11] proposed a theoretical model to predict CHF for pool boiling based on the effects of the contact angle, which is based on material properties, and orientation of the surface. His proposed model for predicting CHF is

$$q''_{max} = \left(\frac{1 + \cos\theta}{16}\right)\left[\frac{2}{\pi} + \frac{\pi}{4}(1 + \cos\theta)\cos\phi\right]^{1/2} h_{fg}\,\rho_v^{1/2}\,[\sigma\, g(\rho_l - \rho_v)]^{1/4} \quad (4)$$

The model uses the same hydrodynamic effects from Equation (3) but replaces the *C* with non-hydrodynamic terms which include the dynamic receding contact angle, θ, and the orientation of the surface, ϕ. A horizontal, upward facing surface is represented by $\phi = 0°$ and a vertical surface is represented by $\phi = 90°$. The contact angle depends on the fluid and surface. The contact angle must be known to estimate a value. Kandlikar reports values using Equation (4) with smaller errors based on experimental data when compared to values found using the *C* with Equation (3). This model should provide a better estimate of CHF, since this model accounts for the orientation of the surface. Kandlikar and Steinke [12] reports the contact angle for a stainless steel surface and water ranges from about 45 to 60 degrees for surface temperatures for 100 to 130 °C and about 130 to 140 degrees for 130 to 175 °C. Assuming a contact angle of 60 degrees, the equivalent CHF constant C using Kandlikar's theoretical model is 0.126 for a horizontal surface and 0.075 for a vertical surface. These values are close to Zuber's and Chang's CHF constants. However, when using a contact angle of 135 degrees, the equivalent C is 0.017 for a horizontal surface and 0.015 for a vertical surface, which are much lower values than Zuber's and Chang's CHF constants.

3 System Design and Setup

The proposed setup is designed to create heat fluxes up to CHF and measure those heat fluxes using the high temperature heat flux sensor (HTHFS). A control system, outside the scope of this work [22], was built to control the heat fluxes to just below CHF. A brief summary of the setup is given here. The following sections further explain in detail the individual parts of the setup; the conceptual and physical design of the entire system, the heat flux sensor, and the heat source.

A two-inch, schedule 80 pipe nipple provides the boiling surface on its outer diameter while heat is applied to the inner diameter, with the HTHFS embedded in the wall of the pipe to directly measure the heat flux, as shown in Figure 2. An electric heater initially is used to provide the heat to the inner diameter of the pipe. An oxy-acetylene torch is used for the final experiments. The pipe is sealed at the bottom to prevent water from leaking in, and the pipe assembly is placed into a can of water and suspended vertically. The cylindrical geometry and vertical position emulates nuclear reactor fuel rods since geometry and configuration of the boiling surface does affect the boiling characteristics as well as CHF and one of the primary applications for this project is for nuclear fuel rods.

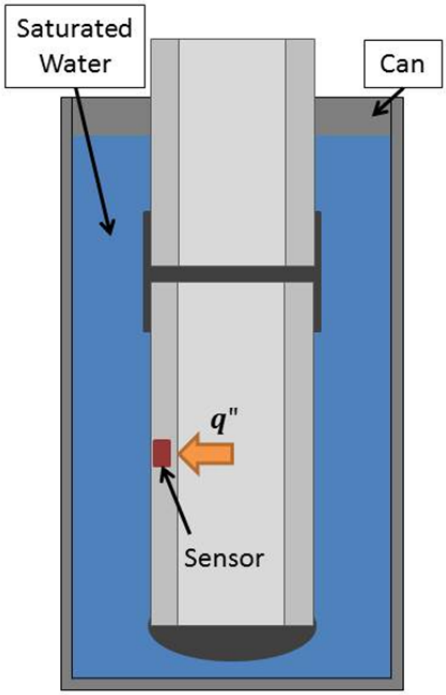

Figure 2. General diagram of the pipe assembly in saturated water. Shows the location of the sensor and where the heat flux is applied.

3.1 Conceptual Design. A vertical cylinder is used to simulate a nuclear fuel rod. Fuel rods usually have a diameter of about 1 cm (0.394 inches), but a larger diameter is used for this setup to allow more room for the heat flux sensor and to easily access the inner diameter to install a heater. While designing the system, a few concerns are investigated before testing. These concerns include:

- How much power is needed to reach CHF
- How fast will the system heat up once CHF occurs
- Can the heater be controlled to prevent burnout
- Is the sensor experiencing one-dimensional heat transfer
- Is the heat flux distribution over the sensor area uniform

The last two bullets will determine if the surface heat flux is accurately measured by the sensor.

3.1.1 Power Requirement. Since heat flux is defined as the heat transfer per unit area, and the heat transfer is dependent on the power input to the heater, a larger area requires more power to produce the same heat flux. Applying heat to the entire area of the pipe could result in an enormous amount of power to reach CHF. In order to select or design a heater that will allow CHF to be reached, the amount of power required must be estimated. The power required by the heater is estimated by

$$P = q = q''_{max}\, A_{heater} \tag{5}$$

The surface area of the heater must be large enough to cover the sensor, but a larger surface area requires more power to get the same heat flux. From Equation (3), using saturated water properties at 100 °C, the maximum heat flux, or CHF, is estimated to be 1105.7 kW/m² using Zuber's CHF constant, C=0.131. By designing the heater to have an area of 1 in², the estimated required power is 873.8 W. This is a feasible amount of power and it should provide enough surface area to cover the sensor.

3.1.2 Temperature Change Rate. Once CHF is exceeded, the surface basically becomes insulated with vapor and the temperature increases drastically up to an extreme value in a short period of time. Since the goal is to reach CHF and eventually to control the heater to CHF, it will be beneficial to know how fast the temperature will increase once CHF is reached. The energy balance of the wall includes the heat input from the heater on the inner diameter, which is assumed to equal the power input to the heater, and the heat output from the surface, which is the heat transferred from the outer diameter to the water. For this transient case the energy balance assumes one-dimensional heat transfer through the wall, and the energy balance equation is

$$P_{in} - q_{out} = \rho \mathcal{V} C_p \frac{dT}{dt} \tag{6}$$

Once CHF is reached, the heat flux output drops dramatically. Since the heat input is still at the level of CHF, the heat output can be assumed to be zero as a worst case scenario. Solving for the temperature change rate will tell how fast the temperature will increase once CHF is reached, which is shown as

$$\frac{dT}{dt} = \frac{P_{in}}{\rho \mathcal{V} C_p} \tag{7}$$

If the heat output isn't zero the temperature change rate is lower, so assuming the heat output to be zero after reaching CHF results in the maximum temperature change rate. Using the required power to reach CHF, the volume of the heated area of the pipe wall, and properties of stainless steel at 300 K, the temperature change rate is calculated to be 58.36 K/s. The actual rate of change is smaller because the specific heat increases with temperature, and because the heat transfer is in the film boiling regime the heat transfer is no longer one dimensional and has three-dimensional heat transfer effects. This means that once CHF is reached there is enough time for a controller to respond and reduce the power to prevent the system from reaching extremely high temperatures.

3.1.3 Numerical Model. A finite-difference model is used to determine if the one-dimensional heat transfer assumption is valid and to determine if the heat flux distribution across the heat flux sensor area is uniform. The model calculates the temperature distribution in a 2-D, uniform wall based on the parameters of the system. The boundary condition for the inner diameter is setup so that the input heat flux is equal to the heat flux from the heater for the heated length and the heat flux for the unheated length is equal to zero. The heat flux boundary condition for the outer diameter, which is the surface, is dependent of the excess temperature. For excess temperatures less than 5 °C the heat flux is due to natural convection (see Appendix A). For excess temperatures higher than 5 °C the heat flux is in the nucleate boiling regime and Rohsenow correlation is used calculating the heat flux based on the surface temperature. The input heat flux is adjusted so that the maximum surface heat flux is approximately equal to CHF. To get CHF at the outside wall, an input heat flux of 104% of CHF is required from the heater.The result also shows that the average heat flux with in the area of the sensor, which is illustrated on Figure 3, is 95% of the input heat flux from the heater. The numerical model also shows the uniformity of heat flux over the sensor area. The variation of the heat flux from the average heat flux over the sensor area is 2%. Based on this information, the assumptions of one-dimensional heat transfer through the sensor and uniform heat flux across the sensor area are valid.

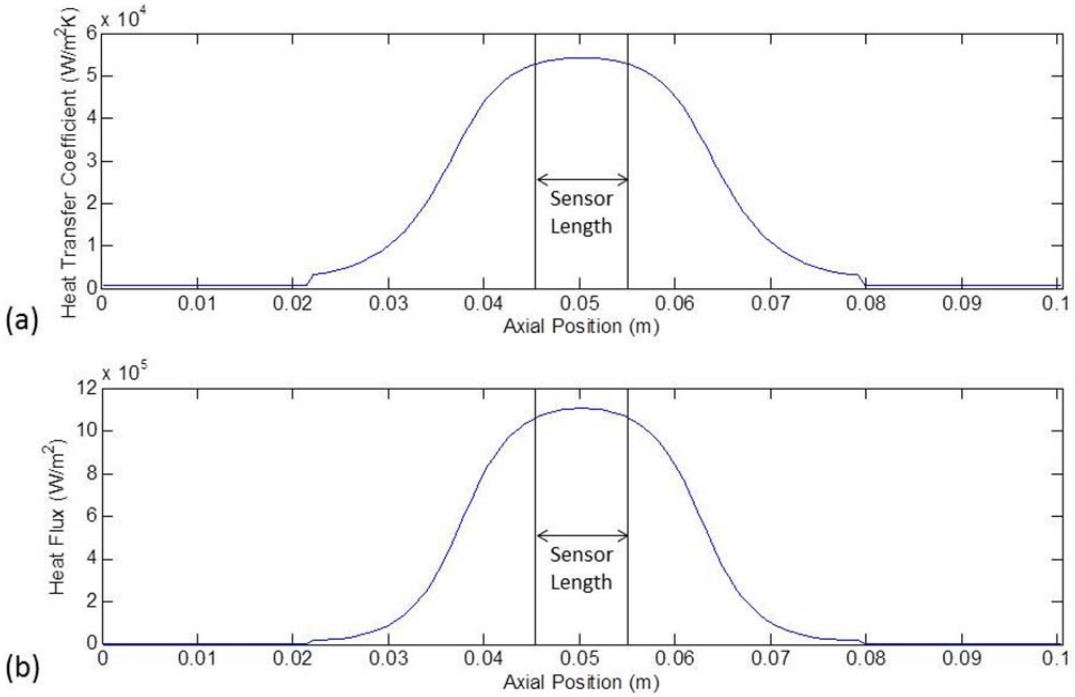

Figure 3. Output plots from the finite difference model showing the distribution of: (a) the heat transfer coefficient, (b) the surface heat flux. The length of the pipe is the axis for the distributions.

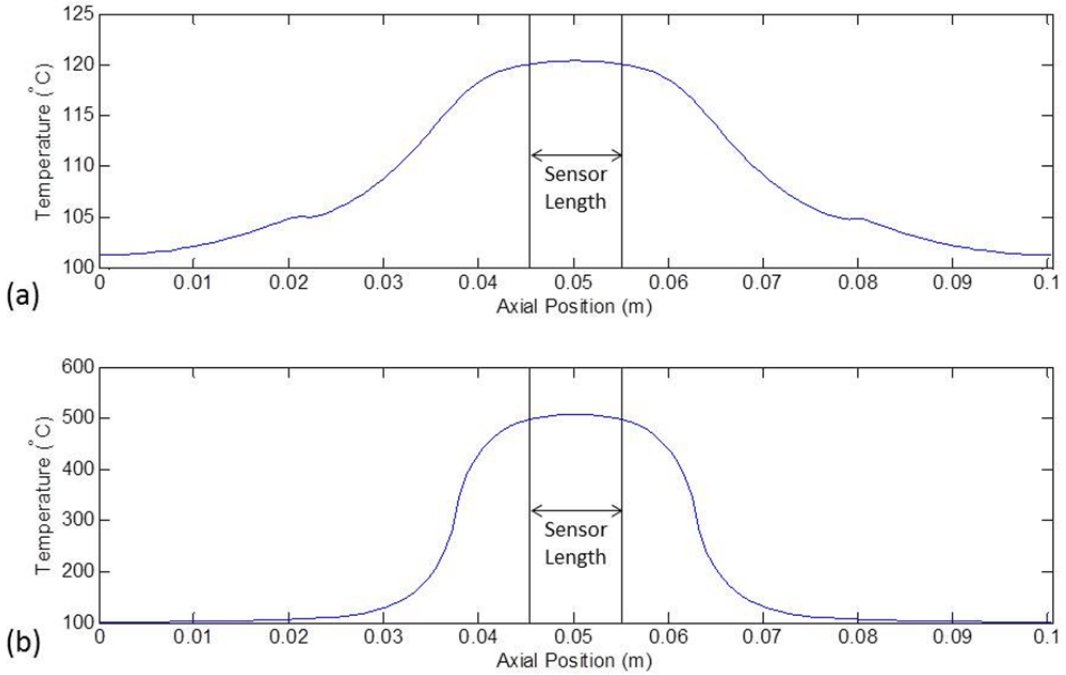

Figure 4. Temperature distribution plots along the length of the pipe for: (a) the outer diameter, (b) the inner diameter and adjacent to the heater. The length of the pipe is the axis for the distributions.

3.2 Heat Flux Sensor. The high temperature heat flux sensor (HTHFS), which was developed by Gifford, Hubble, and Pullins [14], is used to measure the heat flux through the pipe wall. The sensor can operate at temperatures in excess of 1000°C without being water cooled. This is beneficial for this experiment since the temperature in the pipe wall will start to increase quickly once CHF is reached, and the estimated temperature difference across the pipe wall just before CHF is reached is about 390 °C with the maximum temperature being 510 °C, which is calculated from the numerical model. The sensor's design, Figure 5, is based on a thermopile design made of a series of K type thermocouple material junctions through the sensor. A typical sensor has dimensions of 0.38 in × 0.20 in × 0.125 in (length × width × thickness), and has 5 junctions. The sensor gives a direct voltage output that is proportional to the heat flux, and also outputs the top surface temperature, T_1, and bottom surface temperature, T_2.

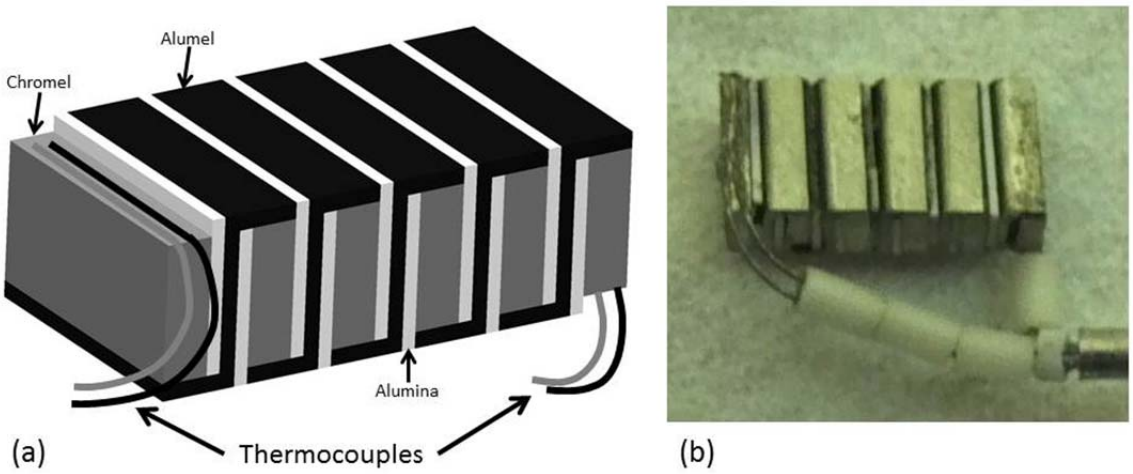

Figure 5. HTHFS used in proposed system: (a) CAD drawing, (b) actual sensor installed in the pipe.

3.2.1 Background. The HTHFS measures heat flux using a hybrid method involving the methods of both a differential heat flux sensor and a slug calorimeter. The hybrid heat flux (HHF) method is introduced by Hubble and Diller [15], and it is summarized in this section.

A differential heat flux sensor measures the temperature difference across a thickness with a known thermal conductivity, as shown in Figure 6a. The heat flux through the sensor is calculated using the steady-state version of Fourier's law.

$$q''_{diff} = \frac{q''_1 + q''_2}{2} = \frac{k}{\delta}(T_1 - T_2) \tag{8}$$

This version of the differential heat flux is for energy flow from the top to the bottom of the sensor, which is the direction for the calibration measurements (Figure 6a). The heat flux into the sensor is labeled as q''_1 and the heat flux out of the sensor is labeled as q''_2. The labels for the heat flux into and out of the sensor are independent the direction of heat transfer through the sensor (from top to bottom or bottom to top). The energy flow is in the opposite direction for the proposed system, in which case the temperature difference will be $(T_2 - T_1)$. For steady-state conditions the net absorbed heat flux into the sensor is equal to the heat flux exiting from the bottom of the sensor. Differential heat flux sensors are best used in near-steady state measurements where thermal storage within the sensor is negligible. It requires the sensor to

have good thermal contact with its mounting surface, and that the heat flux through the sensor is one-dimensional.

A slug calorimeter determines the heat flux by measuring the thermal energy stored in the sensor as a function of time with a known thermal capacitance. The energy balance for the control volume in Figure 6 results in

$$q"_{slug} = q"_1 - q"_2 = \rho C_p \delta \frac{dT_{avg}}{dt} \tag{9}$$

where $\rho C_p \delta$ is the thermal mass per area of the sensor and T_{avg} is the average of T_1 and T_2. Since the rate of change of temperature is needed to calculate heat flux, a slug calorimeter cannot be used for steady state measurements. A slug calorimeter also needs to be insulated from its mounting surface to reduce or eliminate $q_2"$ in order to increase the thermal energy stored.

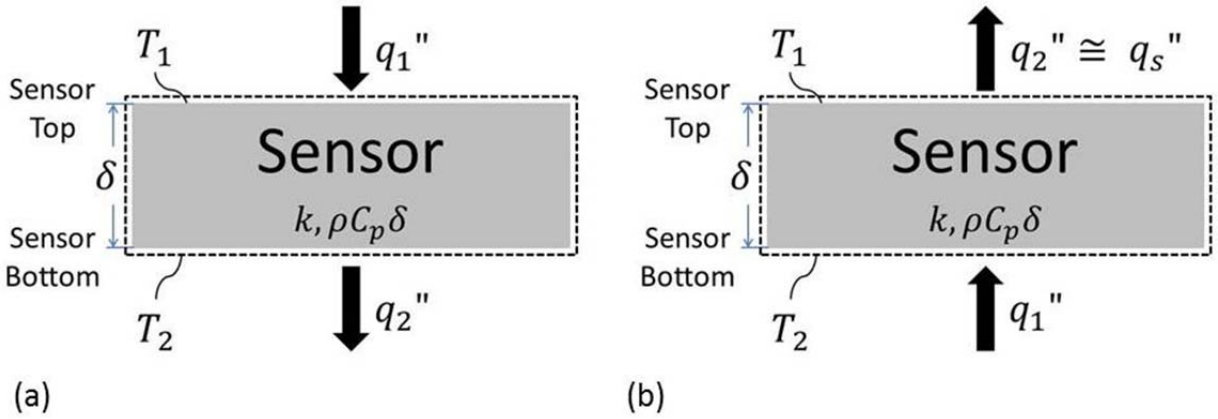

Figure 6. Sensor energy balance diagrams with heat flux and temperature labels: (a) Shows the direction of heat transfer for the calibration setup. (b) Shows the direction of heat transfer for the proposed system setup.

While both methods are useful for certain types of heat flux measurements, their performance is limited to certain backing materials. The HHF method combines the differential and slug heat flux signals to determine the net absorbed heat flux into the sensor in both steady state and transient conditions. Combining Equations (8) and (9) and eliminating $q"_2$ gives

$$q"_1 = q"_{diff} + \frac{1}{2} q"_{slug} \tag{10}$$

The sensor is calibrated with the heat input on the top, so $q"_1$ is the known heat flux for the calibration. The HHF method allows the sensor to be used in any backing material and can measure heat flux accounting for both steady state and transient modes of heat transfer. The HHF method also improves the response time and accuracy of the sensor. The HTHFS is designed to directly output a heat flux signal, which is equal to the differential heat flux, and also outputs the temperatures T_1 and T_2 which are used to determine the slug heat flux.

In the experimental setup, the heat flux of interest is not the entering heat flux $q"_1$ but the leaving heat flux $q"_2$. Combining Equations (8) and (9) and eliminating $q"_1$ gives

$$q"_2 = q"_{diff} - \frac{1}{2} q"_{slug} \tag{11}$$

3.2.2 Mounting. As shown in Figure 7, the HTHFS is mounted in the wall of the stainless steel pipe to provide a measurement of the heat flux through the wall to the water. A 2-inch Schedule 80 pipe has a wall thickness of 0.218 inches which allows enough space for the sensor to be flush-mounted in the wall. A cavity for the sensor is machined in the wall at the center of the length of the pipe, with a channel of a smaller width machined off-center of the cavity to provide a way for the lead wires to exit the pipe. The sensor is placed in the pocket, and the lead wires are strain-relieved using stainless steel sheets spot welded to the Inconel sheath of the lead wires and then to the pipe. A castable ceramic potting material, Ceramacast 675-N manufactured by Aremco [20], is used to fill in the void space of the pocket around the sensor which electrically insulates the sensor from the pipe and thermal and mechanically bonds the sensor to the pipe. A stainless steel sheet is applied over the sensor cavity and bonded to the surface with a ceramic adhesive, Aremco Ceramabond 865 [21], and the sheet is welded to the pipe around the cavity. The ceramic adhesive provides good thermal contact between the stainless steel sheet and ceramic potting material. The stainless steel sheet also provides a smooth, homogeneous boiling surface. Figure 7 illustrates how the heat flux sensor is mounted in the pipe for measurements.

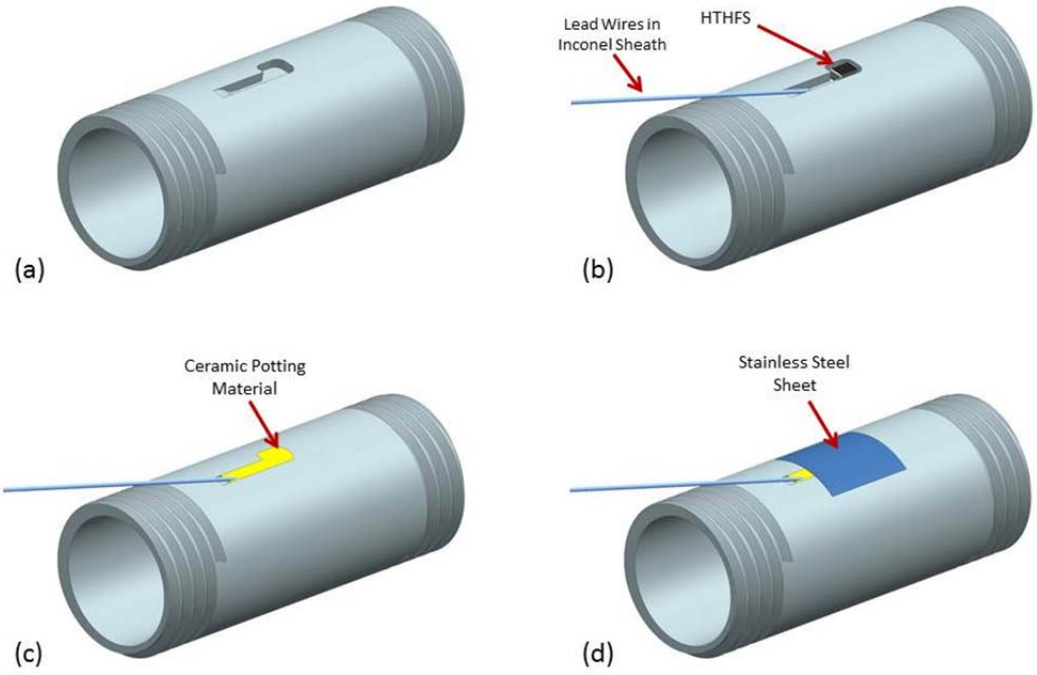

Figure 7. Heat flux sensor mounting drawings: (a) Stainless pipe with sensor cavity. (b) Heat flux sensor mounted in the sensor cavity. (c) Sensor cavity filled with ceramic potting material. (d) Stainless steel sheet bonded and welded to pipe over sensor cavity.

3.2.3 Differential Heat Flux Calibration. Steady state calibrations are performed at room temperature using a halogen lamp for a radiation heat flux source. The halogen lamp's heat flux output is controlled using a variable transformer. A reference, water-cooled Schmidt-Boelter gage, made by Medtherm, is used to determine the incident heat flux from the lamp as a function of the voltage input, which is read using a true RMS multimeter. The reference gage is coated with black Zynolyte paint on the surface for a high emissivity of 0.94.

As shown in Figure 8, the sensor is centered with the halogen lamp to provide a uniform heat flux, and is placed at a distance of 1.25 in from the lamp, the same as the reference gage, using a gage bar for a consistent distance alignment. For differential heat flux calibration, a steady-state condition is required to get an accurate calibration. This requires a cooling source, so a tubing system is constructed to pump cooling water to the sensor area on the inner diameter of the pipe. This is done by attaching a stainless steel tube through a fitting in a PVC pipe cap, which is attached to the pipe, so that the end of the tube is at the center of the pipe and a 90 degree compression fitting creates an impinging water jet against the wall behind the sensor. Since impinging jets have a high heat transfer coefficient, the inside wall behind the sensor remains essentially isothermal. The large size of the lamp relative to the sensor makes the heat transfer essentially one-dimensional. The pipe surface is coated with black Zynolyte paint to give it a high emissivity of 0.94.

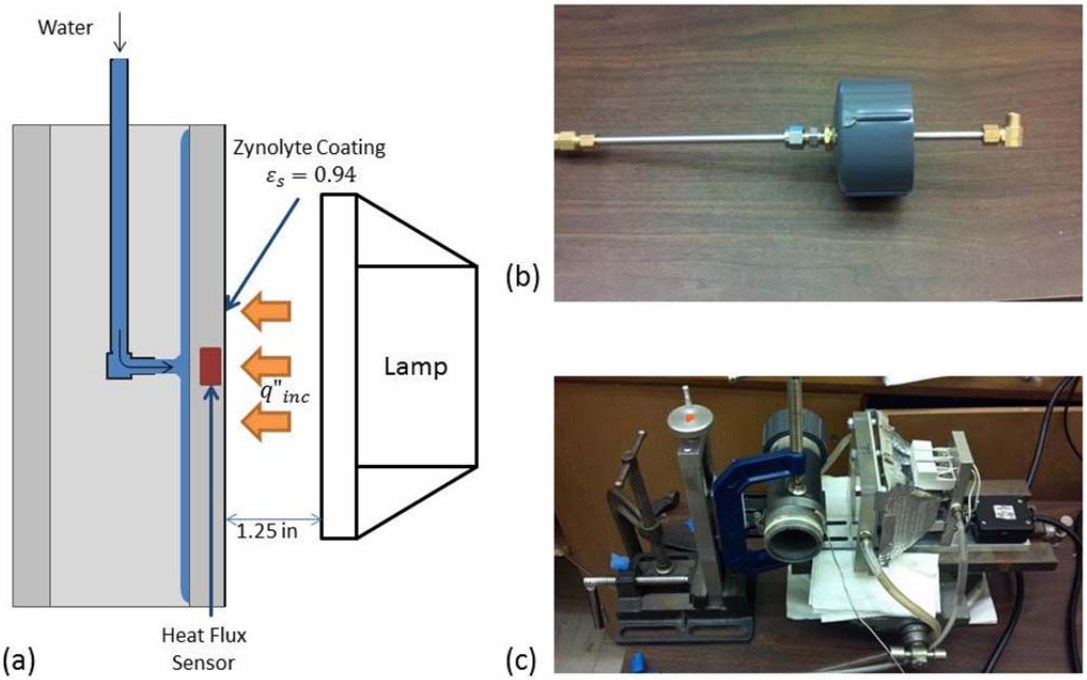

Figure 8. Differential heat flux calibration setup diagrams: (a) Diagram of the top view of the setup, showing a cross sectional view of the pipe with the water cooling system, (b) Steel tubing mounted in a PVC pipe cap used to water cool the heat flux sensor, (c) Complete calibration setup using the halogen lamp (right).

During the calibration process, the power to the lamp is increased incrementally by adjusting the Variac from 40 V to 120 V by 10 V increments. The absorbed heat flux is measured by the sensor at each Variac voltage. The incident heat flux from the lamp is determined from the Variac voltage using

$$q"_{inc} = p_1 V_{var}^4 + p_2 V_{var}^3 + p_3 V_{var}^2 + p_4 V_{var} \quad (12)$$

The relationship between incident heat flux and Variac voltage is determined by measuring the heat flux at each Variac voltage with the reference gage and fitting the results to a polynomial curve. Table 1 gives the values for the polynomials in Equation (12). A high resolution data acquisition device is used to record the voltage output from the sensor. The system is allowed to reach steady state for each step input. The average temperature of the sensor is kept at room temperature by adding ice to the water source. This ensures that the sensitivity of the sensor for each step input is determined at the same temperature.

Table 1. Values for polynomials in Equation (12).

p_1	p_2	p_3	p_4
1.7773×10^{-10}	-5.1537×10^{-7}	1.8497×10^{-4}	2.2517×10^{-3}

For each step input, the average voltage output for each heat flux signal is calculated during the time the signal is at steady state. Each average voltage output corresponds to a known heat flux from the lamp that is determined by the variable transformer voltage and Equation (12). The heat flux measured by the sensor is the absorbed heat flux from the lamp, which is proportional to the incident heat flux shown as

$$q"_{abs} = \varepsilon_s q"_{inc} \quad (13)$$

With the heat flux known, the room temperature sensitivity is calculated from

$$S_0 = \frac{V_{out}}{q"_{abs}} \quad (14)$$

Multiple heat flux levels are measured for the calibration, and the room temperature sensitivity for each heat flux level is averaged to get the true sensitivity.

Room temperature calibrations are performed before and after each set of tests to ensure accurate results for all the tests. A total of four separate calibrations were performed. Table 3 reports the results from the differential heat flux calibrations at the different times they were performed, which occurred before and after each set of tests performed. As shown, the sensitivities do change a little over time and it is hypothesized that the thermal cycling from the tests caused changes in the contact resistances between the stainless steel and ceramic potting material which change the flow of thermal energy through the wall enough to give different output.

A high temperature calibration is used to account for the change in sensitivity with changes in temperature. This change in sensitivity occurs mainly due to changes in thermal conductivity of the sensor materials. The setup and procedure for this calibration is described by Pullins and Diller [16]. The sensitivity as a function of the average temperature, in °C, is shown as

$$S = S_0 \left((4.2787e-10) T_{avg}^3 + (-1.1049e-6) T_{avg}^2 + (3.3712e-4) T_{avg} + 1 \right) \quad (15)$$

The high temperature calibration does not change from sensor to sensor therefore only the room temperature calibration is performed on this heat flux sensor. The high temperature correction presented in Equation (15) is based on previous work. The average temperatures during the testing are greater than 200 °C therefore the temperature needs to be taken into consideration for determining the differential heat flux. The differential heat flux is then determined by

$$q"_{diff} = \frac{V_{out}}{S} \tag{16}$$

where the sensitivity is in μV/(W/cm²) and the signal voltage output is in μV. The calibration analysis is performed for both heat flux signals from the sensor.

3.2.4 Slug Calorimeter Calibration. The thermal mass of the sensor, $\rho C_p \delta$, is determined by performing transient measurements. In order to perform a slug calorimeter calibration the sensor must be insulated in order for the rate of change of temperature term in Equation (9) to be relatively constant. The slug calorimeter calibration cannot be done with the sensor installed in the pipe because it cannot be insulated. Since every HTHFS is built the same, the thermal mass of each sensor should be approximately equal. Therefore the slug calorimeter calibration is done with three identical sensors.

Each sensor used for the transient measurements is mounted in a disc of alumina insulation material with the top of the sensor exposed to the air. The surface of the sensor is coated with Zynolyte for an emissivity of 0.94. The setup is similar to that for the differential calibration, where the sensor is centered with the halogen lamp at a distance of 1.25 in. During the measurement process, the sensor is allowed to remain at an initial temperature, around room temperature, and the lamp is turned on providing a constant heat flux from the lamp. The lamp remains on for about 30 seconds and then is turned off. The sensor is allowed to cool to room temperature and the process is repeated for a higher heat flux level until 3-4 different measurements are obtained.

It can be difficult to perfectly insulate the bottom of the sensor to have $q_2"$ equal zero. The analysis used for determining the thermal mass does not assume that $q_2"$ is equal to zero, and defines the absorbed heat flux due to radiation into the sensor as the net absorbed heat flux from all sources, not just the lamp. Other factors that need to be considered are losses due to convection and re-radiation. Figure 10b illustrates the energy balance of the sensor used for the slug calorimeter calibration analysis, where

$$q"_{conv} = h(T_s - T_\infty) \tag{17}$$

and where

$$q"_{rr} = \varepsilon_s \sigma_{SB} T_s^4 \tag{18}$$

The thermal mass is derived from the energy balance illustrated in Figure 10b and from Equations (9) and (11), which gives

$$\rho C_p \delta = \frac{2\left(q"_{abs} - q"_{rr} - q"_{conv} - q"_{diff}\right)}{\frac{dT_{avg}}{dt}} \tag{19}$$

For the range of data with the lamp turned on, the thermal mass from Equation (19) is calculated for each data point. The calculated thermal mass is plotted versus the time, shown in Figure 9, to determine if the thermal mass is relatively constant. It is seen in Figure 9 that the thermal mass is relatively constant after about 2 seconds. Averaging the values after this time from the data for all three sensors gives $\rho C_p \delta$ =1.042 J/cm²K.

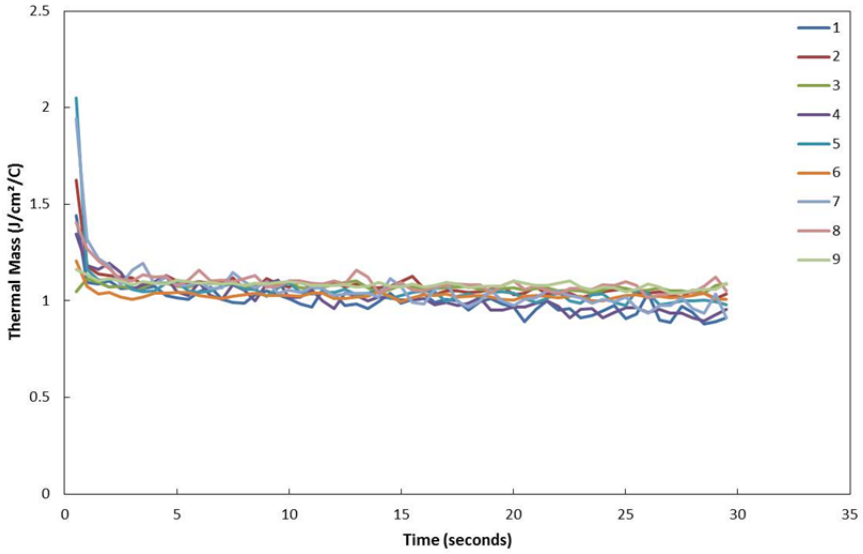

Figure 9. Slug calorimeter calibration plot, thermal mass vs. time, showing the sensor with three separate measurements at different heat flux levels.

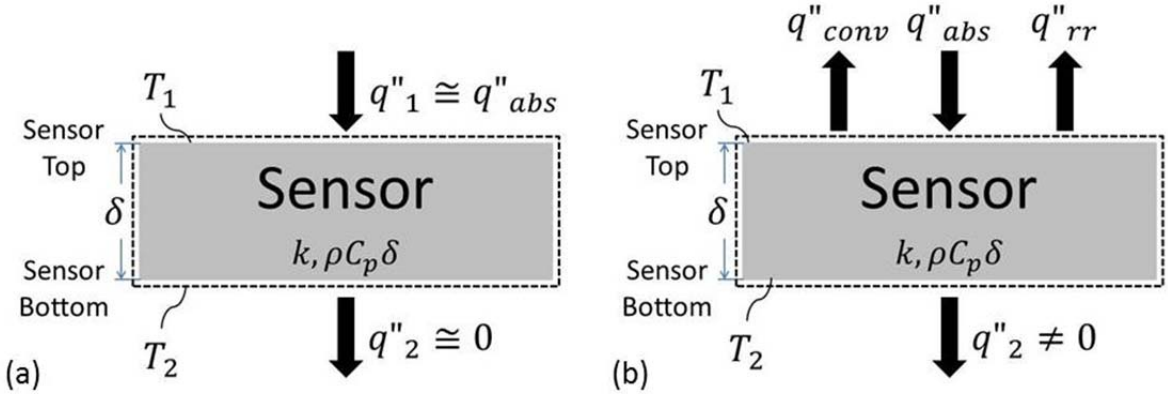

Figure 10. Energy balance diagrams for slug calibration analysis: (a) Energy balance diagram for the previous calibration analysis methods, (b) Energy balance for new calibration analysis method which doesn't assume that $q"_2 = 0$, and includes convection and re-radiation.

3.2.5 Calibration Uncertainty Analysis. Quantities used to determine the room temperature sensitivity have an associated standard uncertainty that contributes the sensitivity uncertainty. The combine standard uncertainty of the sensitivity, $u_c(S_0)$, is determined by using the propagation of error method according to

$$u_c(S_0) = \sqrt{\sum_{i=1}^{N} \left(\frac{\partial S_0}{\partial x_i} u(x_i) \right)^2} \tag{20}$$

where x_i represents a quantity used to determine the sensitivity and $\partial S_0 / \partial x_i$ represents the partial derivative of Equation (14) with respect to each quantity x_i. Standard uncertainties for each quantity are determined either using Type A or Type B evaluation methods. A Type A method is based on statistical

methods and Type B is based on scientific judgment using relevant information such as observation, previous or existing data, or given specifications. The standard uncertainty for each quantity x_i is determined using Type A methods when possible, which is done by calculating the standard deviation of a set of available data. Conservative estimates of uncertainty are determined for quantities that can't be evaluated statistically. When multiple sources contribute to the uncertainty of a quantity the standard uncertainties of each individual source is combined using a root-sum-square method.

The standard uncertainty of the output voltage, V_{out}, is a combination of random and systematic errors. The random error is determined by calculating the standard deviation of the sample of data used to calculate the mean output voltage for each input heat flux. The signal bias error is measured at the beginning of each test when the input heat flux is zero and is removed from the rest of the data, eliminating bias error from the calibration. Another systematic error comes from positioning the sensor to be centered with the lamp. The error due to position is determined by taking experimental measurements at a determined "zero" and moving the pipe and sensor in each direction (up, down, left, right, in, out, rotate clockwise, rotate counterclockwise) and recording the change in the output voltage. It is estimated that the alignment can be zeroed within 1/8 inch for the translational dimensions, except for the distance from the lamp which is estimated to be zeroed within 1/16 inch, and within 10 degrees for the rotational angle. The random and systematic errors are combined using the root-sum-square method.

The standard uncertainty of the incident heat flux is a combination of the errors due to the fluctuation of and uncertainty in measuring the input voltage, V_{in}, which is estimated using the Type B method. The uncertainty of the Schmidt-Boelter gage's sensitivity also contributes to the standard uncertainty of the incident heat flux, which is reported by the manufacturer to be ±1.5%, as well as its output voltage. The propagation of uncertainty is used for determining the standard uncertainty for the incident heat flux due the input voltage, using Equation (12), and also used in determining the standard uncertainty due to the Schmidt-Boelter gage's quantities, and the two incident heat flux uncertainties are combined using the root-sum-square method. The standard uncertainties used for each quantity is presented in Table 2.

Table 2. Standard uncertainty values used in calculating $u_c(S_0)$.

Quantity	Standard Uncertainty, $u(x_i)$	Units
Surface Emissivity, ε_s	0.0289	-
Input Voltage, V_{in}	0.1155	V
Output Voltage, V_{out}	$V_{out} \times 0.0636$	μV
Schmidt-Boelter Voltage, V_{ref}	$V_{ref} \times 0.0051$	μV
Schmidt-Boelter Sensitivity, S_{ref}	9.38	μV/(W/cm²)

The standard uncertainty of the heat flux sensor's sensitivity is multiplied by a coverage factor, κ, to get the expanded uncertainty which gives the 95% confidence interval for the sensitivity. The coverage factor is equal to the student's t-value for the sensitivity's effective degrees of freedom. The effective degrees of freedom, N, is estimated using the Welch-Satterthwaite formula [19] and is estimated to be equal to 50, which equates to a coverage factor of 2.01. The average expanded uncertainty for the sensitivity is approximately ±14.6% and ±15.3% for the alumel and chromel sensitivity respectively.

Table 3. Sensor sensitivities for each calibration with their corresponding uncertainties.

	Parameter	Calibration 1	Calibration 2	Calibration 3	Calibration 4	Units
Alumel-Alumel Signal	Sensitivity, S_0	393.33	301.96	317.17	347.36	μV/(W/cm²)
	Standard Uncertainty, $u_c(S_0)$	28.54	21.89	23.00	25.20	μV/(W/cm²)
	Expanded Uncertainty, $\mathrm{U}(S_0)$	57.36	44.01	46.24	50.65	μV/(W/cm²)
Chromel-Chromel Signal	Sensitivity, S_0	453.30	376.84	272.74	272.90	μV/(W/cm²)
	Standard Uncertainty, $u_c(S_0)$	34.47	28.65	20.75	20.76	μV/(W/cm²)
	Expanded Uncertainty, $\mathrm{U}(S_0)$	69.29	57.58	41.70	41.74	μV/(W/cm²)

The standard uncertainty for the thermal mass from the slug calorimeter calibration is estimated by calculating the standard deviation of the individual thermal masses that are averaged to estimate the average thermal mass of the sensor. The standard uncertainty is estimated to be 0.0614 J/cm²K, which is equal to 6.6% of the estimated thermal mass. While this estimation is only based on the repeatability of the calibration, the effect of the thermal mass on the total heat flux is small compared to the differential heat flux especially when measurements are taken during steady state conditions.

3.3 Electric Heater. An electric resistance heater provides a constant heat flux into the system. An electric heater is easy to use and the heat flux input is controlled by the voltage difference across the heating element. As discussed earlier, the minimum required power is determined to be 870 W. Since this is found under ideal conditions, any non-ideal losses will most likely result in needing more power to reach CHF. To account for this, the heater is sized to give an output of at least 1000 W.

A commercially-manufactured heater that suits the system requirements is not available without a custom order. To reduce cost, an electric heater is designed and built in-house, which allows the heater to be made of materials that will survive the expected high temperatures and sit flush against the inner diameter of the pipe.

The most readily available power source is 120 V with a 15 amp breaker, so the 1000 watt power requirement needs to be achievable with this power supply. The electrical power is

$$P = V\,I \tag{21}$$

The maximum that can be achieved with the voltage and current limits is 1800 W, which provides enough power to achieve the 1000 W that the heater is to be designed for. The heater's resistance is chosen based on the voltage and current limits. The relationship between voltage, current, and resistance is defined by Ohm's law. The electrical power equation rewritten in terms of resistance is shown as

$$P = \frac{V^2}{R} \tag{22}$$

The maximum heater resistance to supply 1000 W at room temperature is 14.4 Ω. If heater resistance is too low the current at 1000 W becomes high, requiring large lead wires. A minimum of 10 Ω is selected as the lower limit.

Another factor to take into account is the change in resistance of the heater element as the temperature increases. This temperature dependence of electrical resistance is approximated by

$$R = R_0[1 + \alpha(T - T_0)] \tag{23}$$

The temperature coefficient of resistance, α, is approximately constant. High temperatures are to be expected for this system up to 1000 °C. The heating element is made from Nichrome 60, a common material for heating elements because of its high melting point (1350 °C) and low cost. Nichrome 60 has a temperature coefficient of resistance of 0.0004 1/°C. A heater with a 10 Ω resistance at room temperature will have a 13.92 Ω resistance at 1000 °C. A heater with a 14.4 Ω resistance at 1000 °C will have a 10.35 Ω at room temperature. The acceptable range of the room temperature resistance is 10-10.35 Ω. This tolerance is small but not unreasonable and the temperature of the heater should not approach 1000 °C until after CHF is reached.

For a given resistance, a variety of different combinations of wire diameter and length can be used. The wire length also has to be able to fit in the approximate 1 in^2 surface area that the heater is designed for. The wire length and size dependence of electrical resistance for a wire is shown in the equation

$$R = \frac{r\,L}{A_c} = \frac{r\,L}{\frac{\pi}{4}D^2} \tag{24}$$

The electrical resistivity is a material property and is equal to about 1.11e-6 Ωm for Nichrome 60 at room temperature. The cross sectional area is determined by the gauge size of the wire. By choosing a variety of wire gauge sizes, the required length of the wire is determined by solving for the length L in Equation (24). A smaller wire requires a shorter length of wire, but since the surface area is proportional to the length and diameter, the surface area will also be smaller. For a constant output power, the surface area and temperature difference are inversely proportional which means that a smaller surface area requires a larger temperature difference ultimately resulting in the wire temperature being larger. To minimize the wire temperature, the surface area must be as large as possible. Since the surface area of the heater is designed to be about 1 in^2, the surface area of the heater wire should be about the same. Wire gauges ranging from 18 to 36 are selected for comparison and it is found that for a 10 Ω resistance heater a 28 gauge wire provides a surface area of 1.13 in^2 and the required length is 28.5 in. While the required length is not extremely long it does present a challenge to fit in the 1 in^2 area of the heater. Drafting software is used to determine if the 28.5 inch heater wire fits in the 1 in^2 area and the wire does fit within the given area, as seen in Figure 11, but does require careful construction do to the small spacing between the rows of wire. One wire size smaller, 30 gauge, results in a surface area of 0.56 in^2 and a length 18.0 in. The length is much shorter which allows more room for the wire to fit in the 1 in^2 area but the surface area of the wire is about half that of the 28 gauge wire, which means that the temperature difference will be double. One size larger, 26 gauge, results in a surface area of 2.27 in^2 and a length of 45.4 in. The doubled surface area is beneficial but the increase in length makes it impossible for the wire to fit within the given area of the heater. Therefore, the 28 gauge wire is the best option to use for the heating element. As seen in Figure 11 the 28 wire fits within the 1 in^2 area but has small clearances for the wire to fit without connecting in places where not desired.

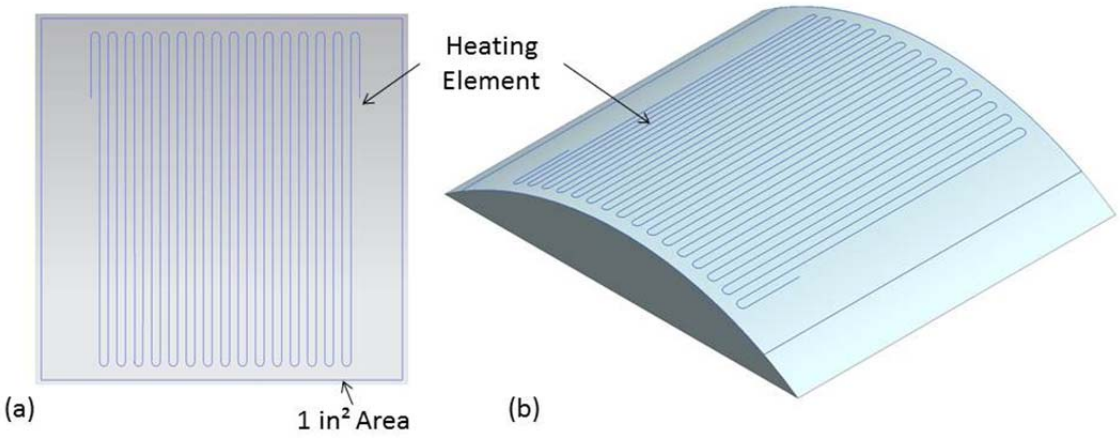

Figure 11. Drawings showing the design of the heating element and sizing: (a) 28.5 in length of wire within the square inch surface area, (b) heating element placed on heater surface area.

The heating element is potted in Ceramacast which provides electrical insulation from the pipe wall and also provides good thermal contact between the heating element and the heater surface. A steel frame for the heater is designed to protect the heating element and ceramic potting material from breaking and to allow the heater to be mounted in the pipe more easily. The steel frame, illustrated in Figure 12, has the same curvature as the inner diameter of the pipe and has a channel machined out for the heating element and potting material. Spaces are included on the ends for the lead connectors.

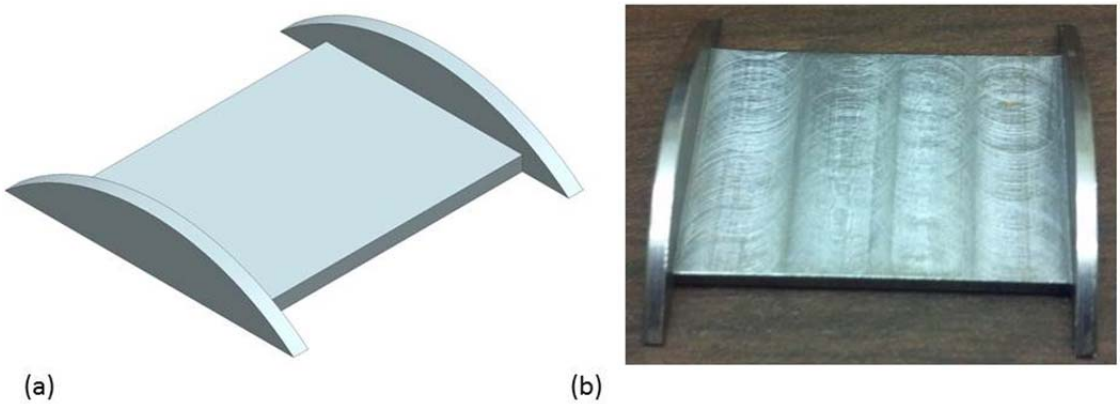

Figure 12. Steel heater frame illustrations: (a) CAD model, (b) actual frame used for one heater.

A jig is created to easily shape the wire to the desired shape, which could be done repeatedly for multiple wires. The jig, illustrated in Figure 13, consists of a wooden block with 0.025 in diameter holes drilled in a pattern so that the holes line up where the bends of the wires are in the concept drawing. Pins are inserted into the holes which allow the wire to be guided around the pins so that the bends are at precise locations resulting in the desired shape. After shaping the entire length of the wire it is removed from the jig and the bends are crimped smaller using pliers, but not so much that the wire is kinked. This allows the straight lengths of the wire to be close together without touching. The wire is then transferred to a piece of tape where its shape can be held in place to be potted in the ceramic within the heater frame.

Two stainless steel strips are then welded to the ends of the wire to serve as lead connectors for the power supply.

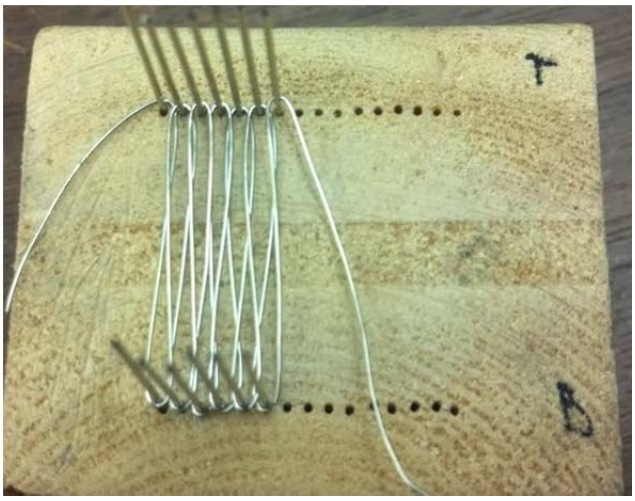

Figure 13. Heat wire jig used to bend the heating element into shape with a partially complete heating element.

A PVC pipe of the same size as the steel pipe used for the proposed setup is used for assembling the heater. The PVC pipe is cut in half so the inner diameter is accessible. The tape strip with the heating element is placed on the inner diameter of the pipe, and held down in place with tape. The heater frame is placed on top of the heating element so that the wires do not touch the frame, and the tape holds the frame in place. The ceramic potting material is inserted through a small hole of the back of the frame using a syringe until the ceramic potting material comes out the sides where the lead connectors are. The potting material is allowed to dry for 8 hours, and the heater is removed and cured in an oven. Once complete the heater surface is sanded smooth so that it is flush with the sides of the heater frame and the heater is ready to be used.

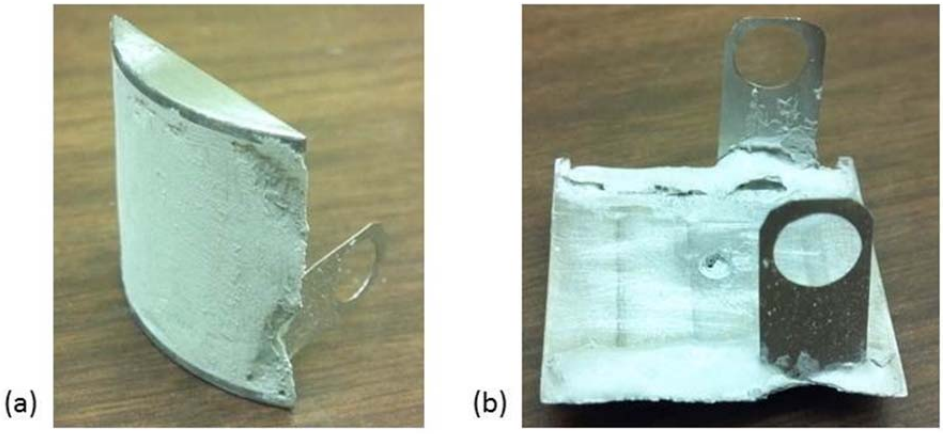

Figure 14. Finished heater pictures: (a) front/side view showing heater surface area, (b) back side of heater showing lead connectors.

3.4 Experimental Setup. The final setup consists of the stainless steel pipe assembly with the embedded heat flux sensor, the heat source, and the can used to hold the water. The heat source used is either the electric heater or the acetylene torch. The setup also includes a hot plate used to pre-heat the water in the can to saturation temperature. To use the electric heater, it is coated with a thin layer of Ceramabond and placed just behind the sensor on the inner diameter of the pipe. The adhesive ceramic allowed to dry for a few hours and cured in an oven before use. High temperature lead wires are attached to the supply power to the heater and run out the top of the pipe. The bottom end of the pipe is sealed with a cap and for the top end a coupling and a short pipe nipple is attached to keep water from getting inside the pipe. For testing, the pipe is submerged in the can of water and held in place by a clamp. The final experimental setup using the electric heaters is illustrated in Figure 15a. When the acetylene torch is used, the overall setup is the same except one modification is made to the pipe to accurately position the flame so it heats the area behind the sensor at a perpendicular angle. A 3/8 in NPT threaded hole is added on the backside of the pipe just behind the sensor. A short pipe nipple is attached and placed through a hole in the can to provide access to the inside diameter of the pipe. All holes are sealed around the pipe nipple to prevent water from leaking out. The cap, coupling, and extension pipe nipple are still used to prevent water from entering through the ends of the pipe.

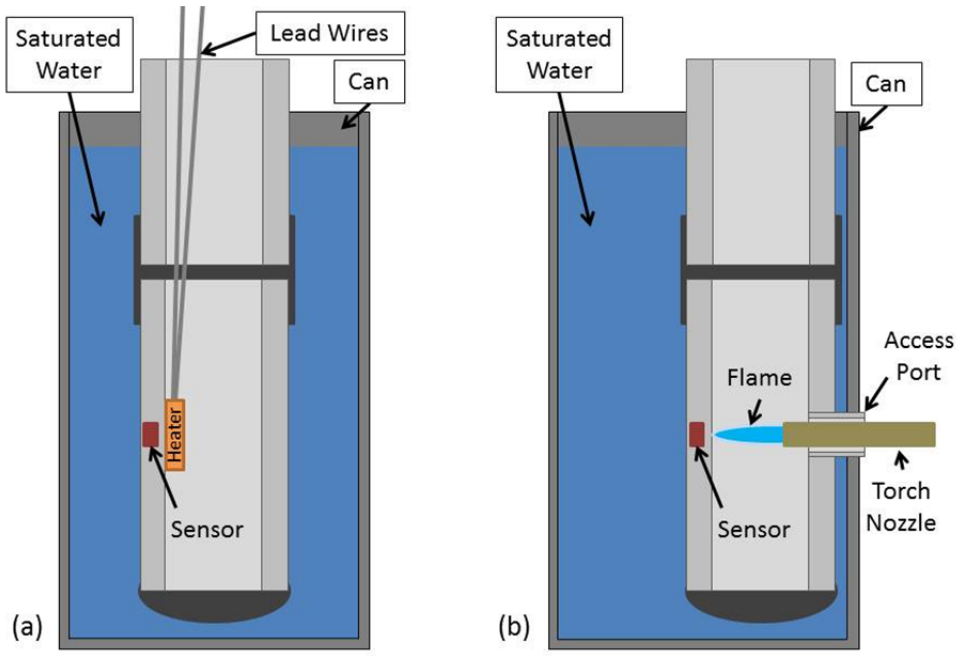

Figure 15. Diagrams illustrating the experimental setup when using: (a) electric heater, (b) oxy-acetylene torch.

4 Experimental Procedure

4.1 Electric Heater. The experiments are performed with the pipe assembly submerged in water. An aluminum can is used to hold the water with the pipe assembly suspended into the can. Since boiling won't occur until the bulk temperature is close to the saturation temperature, the water is preheated using a hotplate. Data is collected using LabVIEW^{TM} software and a high resolution, 24-bit DAQ hardware at a sampling frequency of about 33 Hz. Power is supplied to the heater by a variable transformer, or Variac, which controlled the max power the heater could output. The power to the heater is also controlled by a voltage output signal from LabVIEW^{TM}, which turned off/on the power to the heater once the heat flux voltage reaches a set level and also has a temperature limit to prevent the temperature from increasing if CHF is reached.

Before the testing began, initial measurements are taken to get a zero heat flux measurement which is used to remove signal bias. The temperature limit is initially set to about 200 °C, which is measured by the top thermocouple (TC1) of the heat flux sensor, and the heat flux control set point is initially set to 500 μV, which is approximately equal to 1.5 W/cm². The variac is then initially set to between 15-20 V, at which then the heater is turned on and heat output rises until the heat flux sensor reaches the set point. Once the heat flux set point is reached, the heat flux is kept at the set point for about one minute and then the heat flux set point is raised by 500 μV. The one minute wait after reaching a new the set point allows the system to reach a steady state. The voltage of the variac is increased by about 10 V when there is not enough power to reach the heat flux set point. If the temperature limit is reached and CHF hasn't been achieved, then the temperature limit is increased by 10-20 °C when needed. The heat flux set point is continued to be increased by increments of 500 μV every one minute until CHF is reached or the heater burns out.

4.2 Oxy-Acetylene Torch. To achieve higher heat fluxes, an oxy-acetylene torch is used after performing tests with the electric heater. The flame temperature of an oxy-acetylene torch is approximately 3100 °C, which provides more than enough heat flux to achieve CHF. Data is collected using LabVIEW^{TM} software and the high resolution DAQ at a sampling frequency of 2 Hz. The only means to control the heat flux level is by changing the distance between the flame and pipe wall. Using the modified setup shown in Figure 15, the torch is inserted through the wall of the can and pipe and is moved closer to the wall to increase the heat flux. For consistency, a custom torch stand is made to hold the torch handle steady with the tip at the same height at the access hole in the water can. The torch stand can move across the table so the torch tip can move closer to the pipe wall.

Just like the electric heater tests, initial measurements for the zero heat flux signal are taken to remove signal bias for the data analysis. A hotplate is used to preheat the water in the can close to saturation temperature. The torch is lit and inserted into the access hole and placed at a distance of about 1.75 in from the pipe wall. After the system reaches a steady state, the tip is moved 1/8 in. closer, and the process is repeated until CHF is reached. CHF is determined by observing the temperature and heat flux signals of the sensor. The temperature begins to increase and the heat flux signal begins to decrease once CHF is reached.

5 Data Analysis

While the surface heat flux is directly measured, the surface temperature is not directly measured in the experimental setup. Since there is material between the sensor and the water there is an unknown thermal resistance so the top sensor temperature (TC1) cannot be assumed to equal the surface temperature. Also the surface coefficient $C_{s,f}$ isn't exactly known for this system. While $C_{s,f}$ varies greatly for various surfaces and conditions, the form of Equation (1) has been shown to be valid over a wide range of conditions within the nucleate boiling regime. A data analysis model is developed to calculate the wall thermal resistance and $C_{s,f}$, assuming one-dimensional heat transfer, by using the measured heat flux data in the nucleate boiling to find a value for wall thermal resistance and $C_{s,f}$ that provides a good fit to the data. Once found the wall thermal resistance can be used for data outside the nucleate boiling regime to find the surface temperature.

The surface temperature can be derived from the heat flux from the surface. The convective heat flux from the surface is

$$q"_s = h(\Delta T_e) = h(T_s - T_{sat}) \tag{25}$$

By setting Equation (25) equal to the Rohsenow correlation in Equation (1), the heat transfer coefficient is found to be proportional to the excess temperature squared, and it includes the unknown surface coefficient $C_{s,f}$. As a result, the heat transfer coefficient cannot be determined and the surface temperature cannot be found from Equation (25).

While the installed sensor is used to directly measure the surface heat flux, it is actually measuring the conductive heat flux through the wall to the water, $q"_2$, defined by Equation (11). The heat transfer through the wall is determined to be nearly one-dimensional which means that the conductive heat flux is assumed to be equal to the convective surface heat flux. The heat flux through the layer between the sensor and the surface is

$$q"_s = \frac{1}{R"_w}(T_1 - T_s) \tag{26}$$

The temperature T_1 is measured by TC1 of the sensor. The unknown thermal resistance between the sensor and water is introduced in Equation (26), which replaces the thermal conductivity and layer thickness of the layer between the sensor and surface due to its complex shape and mix of different materials. This thermal resistance can be assumed constant because it is based on the properties of the solid materials in the insulating layer and the temperature doesn't change significantly within the nucleate boiling regime. A least squares curve fit model is introduced to determine the thermal resistance. With the thermal resistance, the surface temperature can be calculated.

The conductive and convective heat fluxes are assumed equal due to the one-dimensional assumption. Therefore Equations (25) and (26) can be combined to get an equation for the heat flux from the sensor to the water, which is shown as

$$q"_s = \frac{1}{R"_{tot}}(T_1 - T_{sat}) \tag{27}$$

where

$$R"_{tot} = R"_w + \frac{1}{h} \tag{28}$$

Figure 16 illustrates the thermal resistance layers used in Equations (26) and (27) along with the corresponding temperature differences. Equation (27) includes the unknown thermal resistance that is

needed for the least squares model, but also includes the heat transfer coefficient which is a function of surface temperature. Substituting Equation (28) into Equation (27) and rearranging the terms results in

$$R"_w\, q"_s + \frac{q"_s}{h} = (T_1 - T_{sat}) \tag{29}$$

The $\frac{q"_s}{h}$ term is equal to the excess temperature, which is seen in Equation (25). Using data from the nucleate boiling regime to determine the thermal resistance, the excess temperature can be determined from Equation (1). All of the terms in Equation (1) are constants except for the excess temperature. The equation can be simplified by replacing all of the constant terms with one coefficient making the nucleate boiling heat flux equal to

$$q"_s = c\,(\Delta T_e)^3 = c\,(T_s - T_{sat})^3 \tag{30}$$

where

$$c = \mu_l\, h_{fg} \left[\frac{g(\rho_l - \rho_v)}{\sigma}\right]^{1/2} \left(\frac{C_{p,l}}{C_{s,f}\, h_{fg}\, Pr_l^n}\right)^3 \tag{31}$$

The excess temperature can be solved from Equation (30) and can be substituted for the $\frac{q"_s}{h}$ term in Equation (29) which results in

$$(T_1 - T_{sat}) = R"_w\, q"_s + \left(1/c\right)^{1/3} (q"_s)^{1/3} \tag{32}$$

The coefficient c is unknown since $C_{s,f}$ is unknown. The coefficients $R"_w$ and $\left(1/c\right)^{1/3}$ are calculated by using the least squares analysis method. The surface coefficient is determined by using the calculated coefficient c in Equation (31) and solving for the surface coefficient. The surface temperature is solved from Equation (26), but the excess temperature is desired more than the actual surface temperature so the saturation temperature is included and the excess temperature is then equal to

$$\Delta T_e = (T_1 - T_{sat}) - R"_w\, q"_s \tag{33}$$

where T_1 and $q"_s$ are values measured experimentally and where T_{sat} and $R"_w$ are constants. The excess temperature is then used for plotting heat flux data vs. excess temperature to create the boiling curve for the proposed system.

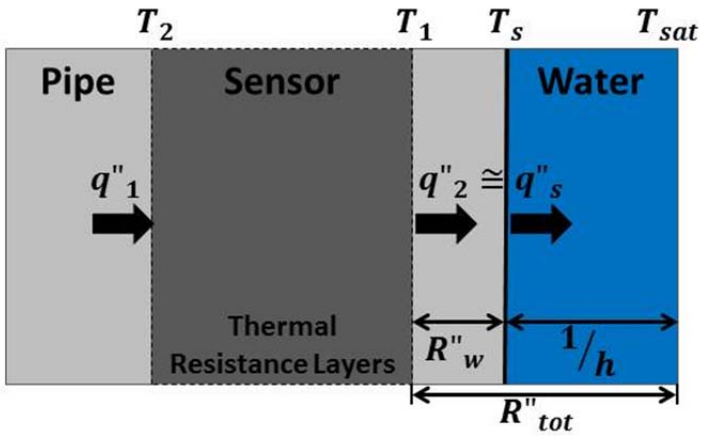

Figure 16. System diagram showing the thermal resistance layers used in the data analysis with their corresponding temperature differences.

The proposed analytical model is limited to a certain range of experimental values. The model uses Rohsenow's correlation for nucleate boiling. Therefore only data points in the nucleate boiling regime can be used, and any data points in the natural convection, transition, and film boiling regimes are excluded. The Rohsenow correlation also assumes that the heat flux and heat transfer coefficient increases with the excess temperature consistently until CHF is reached. Based on existing experimental results the boiling curve has an inflection point before CHF is reached where the heat transfer coefficient begins to decrease with further increase in excess temperature. The Rohsenow correlation does not apply beyond this point. The same is true for the model in Equation (32). The total thermal resistance, from Equation (28), is used to determine what portion of the data can be used for the model since it can be calculated from experimental data. The total thermal resistance decreases with increasing temperature when the heat transfer coefficient increases with temperature, as shown in Figure 17. Plotting the total thermal resistance versus the measured temperature shows if and when the heat transfer coefficient begins to decrease, and that portion of the data is excluded from the analysis model.

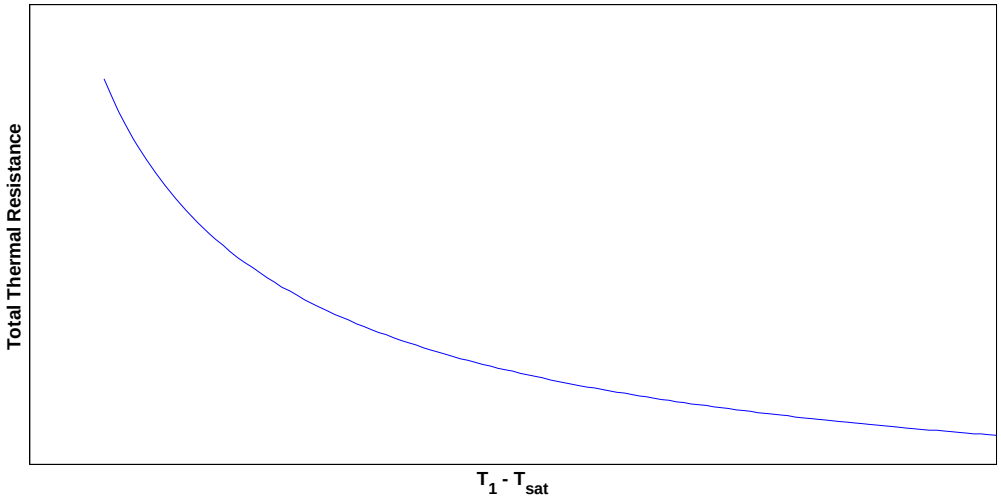

Figure 17. Ideal total thermal resistance vs. T_1-T_{sat} plot for the nucleate boiling regime. The range of data that follows this trend can be used to apply the data analysis model to find R''_w and c.

The heat transfer coefficient is determined using the calculated excess temperature. Rearranging the terms in Equation (25) the heat transfer coefficient is equal to

$$h = \frac{q''_s}{\Delta T_e} \tag{34}$$

Equation (34) can be applied to the entire range of data. By doing so it can be observed how the heat transfer coefficient changes with temperature. The heat transfer coefficient is useful parameter for determining the thermal resistance of the fluid at the surface.

6 Experimental Results

The following sections present the experimental results collected from the proposed setup and are separated based on the heat source used, which is the electric heater and the oxy-acetylene torch. Two different experiments are performed with the electric heaters; the first with a coating of Zynolyte high

temperature paint on the surface and the second without a Zynolyte coating. Four separate experiments are performed with the acetylene torch, with all four having a plain stainless steel surface with no coating.

6.1 Electric Heater Results. The surface heat flux for each set of data is determined by using the collected temperature and heat flux voltage data with Equations (11) and (16). The saturation temperature is measured using a standard thermometer, which is used to determine the fluid properties and calculating the excess temperature. The measured saturation temperature for test 1 and 2 is 98.30 °C and 98.45°C respectively. The calculated heat flux and the two sensor temperatures, measured by TC1 and TC2, are available before applying the data analysis procedure to the data. The measured heat flux data vs. the measured temperature T_1 is illustrated in Figure 18 for both electric heater tests. Both test results show a similar response with relatively little difference with the heat flux at the same temperature difference. The differences between the two data sets are accounted for by considering that the surface conditions are different for each test. The maximum heat flux achieved for Test 1 and Test 2 is 394 kW/m² and 429 kW/m² respectively. The corresponding total temperature difference, which is the difference of between the temperature of TC1, T_1 and the saturation temperature, for each maximum heat flux is 139.5 °C and 131.5 °C for Test 1 and Test 2 respectively. Based on experimental data published in the literature for pool boiling, these temperature differences far exceed the typical excess temperatures for nucleate boiling. This confirms the hypothesis that the temperature measured by TC1 is not equal to the surface temperature. The response from each data set does follow a trend that is expected for this system, and the trend is consistent for the entire range of data collected. The maximum heat flux for each test is the final measured response of the system before the heaters burned out.

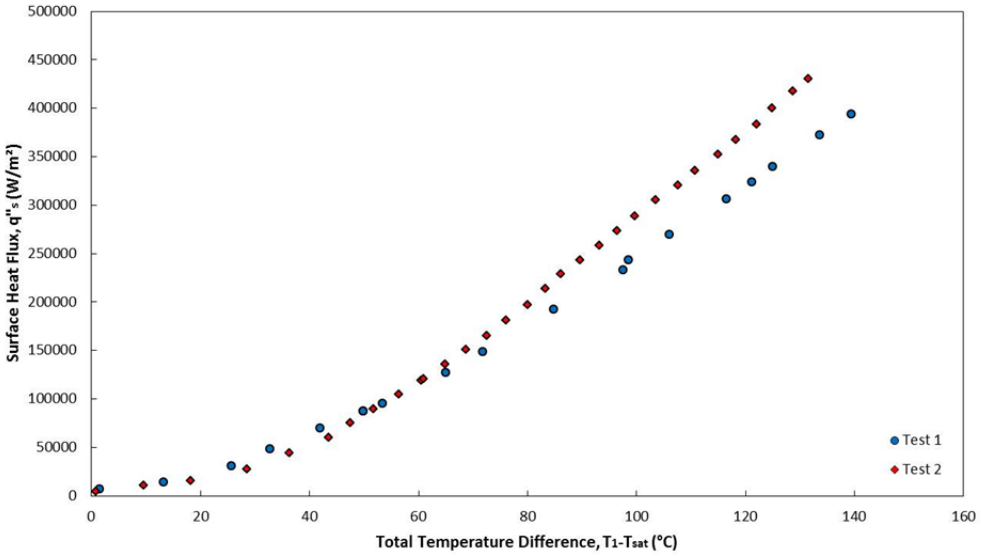

Figure 18. Measured heat flux vs. total temperature difference curves for tests 1 and 2.

The total thermal resistance from the top of the sensor to the water, illustrated in Figure 16, is calculated using Equation (27) with the available measured data. The total thermal resistance is a combination of the thermal resistances of the wall and the inverse of the heat transfer coefficient. While the separate thermal resistance terms are not known before applying the data analysis method outlined in Section 5, the behavior of the heat transfer coefficient with change in temperature can be observed from

the total thermal resistance vs. total temperature difference illustrated in Figure 19. The wall thermal resistance is assumed constant for the nucleate boiling regime. Therefore the total thermal resistance can only change with changes in heat transfer coefficient. The relationship between the total thermal resistance and heat transfer coefficient is shown in Equation (28). As the heat transfer coefficient increases, the total thermal resistance decreases, and vice versa. After about 20 °C, the total thermal resistance for both tests shows a decreasing trend similar to the ideal trend illustrated in Figure 17. This means that the range of data after 20 °C can be used for the data analysis method. The data illustrated in Figure 19 also shows no inflection in the heat transfer coefficient, where it begins to decrease with temperature. This means that the entire range of data after 20 °C is in the nucleate boiling regime and follows the theoretical heat flux model, Equation (30), for a given surface coefficient.

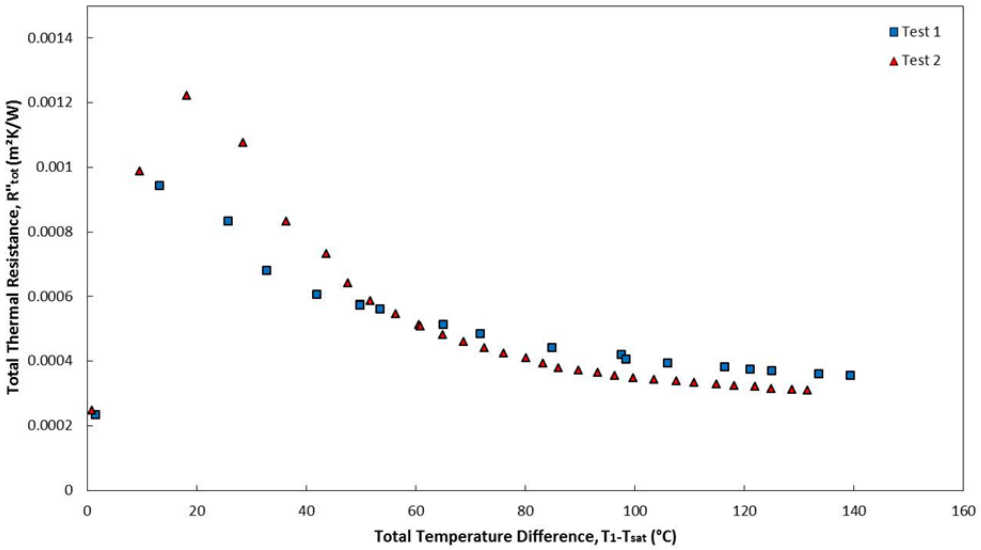

Figure 19. Total thermal resistance vs. total temperature difference curves for tests 1 and 2.

The wall thermal resistance and proportionality constant *c* are calculated using the least squares curve fit model outlined in Section 5. The values for the wall thermal resistance and constant c for each test are presented in Table 4. The excess temperature is calculated using Equation (33). The measured heat fluxes are plotted versus the calculated excess temperatures to create the partial boiling curve for this system, which is illustrated in Figure 20. While the heat flux data correlated similarly in Figure 18, a difference between the two tests can clearly be seen when plotted versus the excess temperature, illustrated in Figure 20. This is due to the difference in the proportionality constant, *c*. Since the saturation temperatures are nearly the same for both tests, the fluid properties (Table 5) are nearly the same. The difference in the proportionality constants is a result of different values for the surface coefficient, which can be calculated from Equation (31). The surface coefficient for each test is presented in Table 4 as well. It can be seen from the Rohsenow correlation for heat flux that a higher surface coefficient is linked to a higher excess temperature for the same heat flux, and this can be seen in Figure 20. The different surface coefficient between the two tests can be justified with the fact that the surface conditions are different, as described earlier.

The proportionality constant also generates theoretical curves for the given surface coefficients. Using Equation (30) the theoretical heat flux is plotted versus excess temperature against the measured data. As

expected, the data correlates with the theoretical curve closely for the range of values measured. This means that the heat flux data collected follows the cubic relationship with the excess temperature fairly closely for this range of values, and it can be seen that an inflection of the heat transfer coefficient has not occurred. Using Equation (34) the heat transfer coefficient is calculated and is illustrated in Figure 21. The heat transfer coefficients calculated from measured data is shown along with their corresponding theoretical curves. The data points follow the theoretical trend fairly closely and confirm that no inflection due to a change in heat transfer coefficient and partial film boiling has been experienced yet.

Table 4. Calculated results determined from electric heater test data.

Parameters	Test 1 Values	Test 2 Values	Units
Max Surface Heat Flux, $q"_s$	393970	429354	W/m²
Wall Thermal Resistance, $R"_w$	0.000238	0.000159	m²K/W
Proportionality Constant, c	3.6996	1.7322	(W/m²)K³
Surface Coefficient, $C_{s,f}$	0.0430	0.0555	-
Max Excess Temperature, ΔT_e	45.75	63.24	°C
Zynolyte Coating	Yes	No	-

Table 5. Parameters used for calculating the surface coefficients for tests 1 and 2.

Parameters	Test 1 Values	Test 2 Values	Units
Saturation Temperature, T_{sat}	98.3	98.45	°C
Gravitational Acceleration, g	9.807	9.807	m/s²
Dynamic Viscosity, μ_l	2.84×10^{-4}	2.86×10^{-4}	Pa·s
Liquid Density, ρ_l	959.34	959.46	kg/m³
Vapor Density, ρ_v	0.5627	0.5678	kg/m³
Surface Tension, σ	0.0592	0.0592	N/m
Enthalpy of Vaporization, h_{fg}	2261.32	2260.59	kJ/kg
Specific Heat, $C_{p,l}$	4.215	4.215	kJ/(kg K)
Prandtl Number, Pr_l	1.78	1.78	-
Fluid-Surface Exponent, n	1	1	-

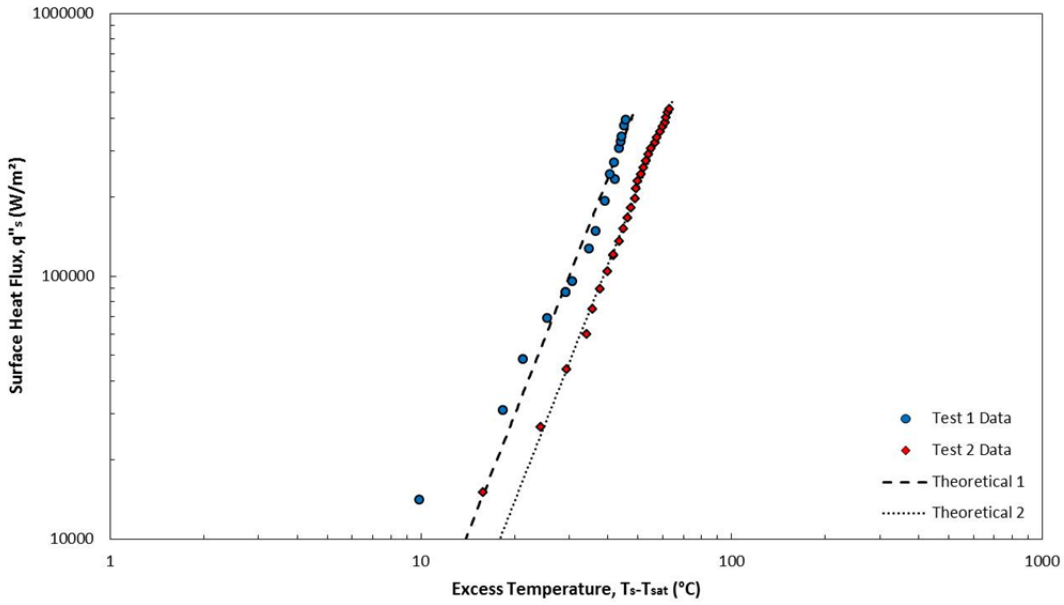

Figure 20. Experimental log-log boiling curves (measured heat flux vs. excess temperature) for tests 1 and 2. Curve fit lines are determined using the heat flux model equation with the constant c calculated from the data analysis method.

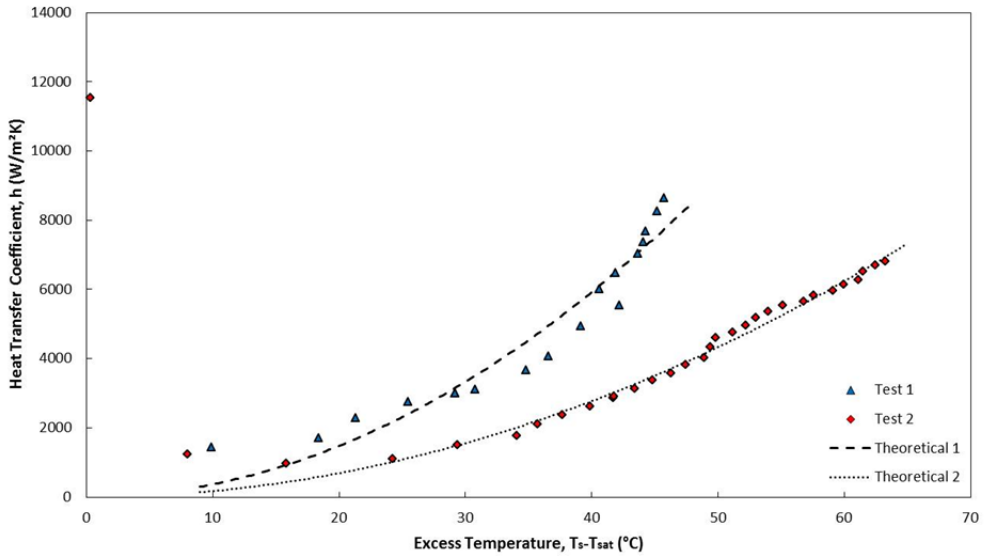

Figure 21. Heat transfer coefficient vs. excess temperature curves for tests 1 and 2.

6.2 Torch Test Results. Experiments are performed using an oxy-acetylene torch in order to reach CHF since the electric heaters are unable to produce high enough heat fluxes without burning out. Heat fluxes from the flame of an oxy-acetylene torch at the tip are on the order of 100 W/cm² which is about what the predicted CHF is calculated to be. A plain stainless steel pipe is initially tested to determine if the pipe is able to survive. During the test, the pipe wall is able to get hot enough to turn red even when submerged in water. The surface had to be a minimum of 500 °C in order to turn red, and the only way for the surface to be that hot is that the surface heat flux is in the film boiling regime. The pipe is also able to survive the test even with CHF being reached. Using the modified experimental setup for the torch and the procedure explained in Section 4.2, four tests are performed in order to get enough data to determine is the results are repeatable. All four tests are performed with no Zynolyte coating. For each test, it is observed that at a certain point the heat flux signal dropped and the measured temperatures increased at the same instant. Figure 22 illustrates this phenomena occurring for one test, which occurs in this case at around 378 seconds. This point is classified as CHF for each test.

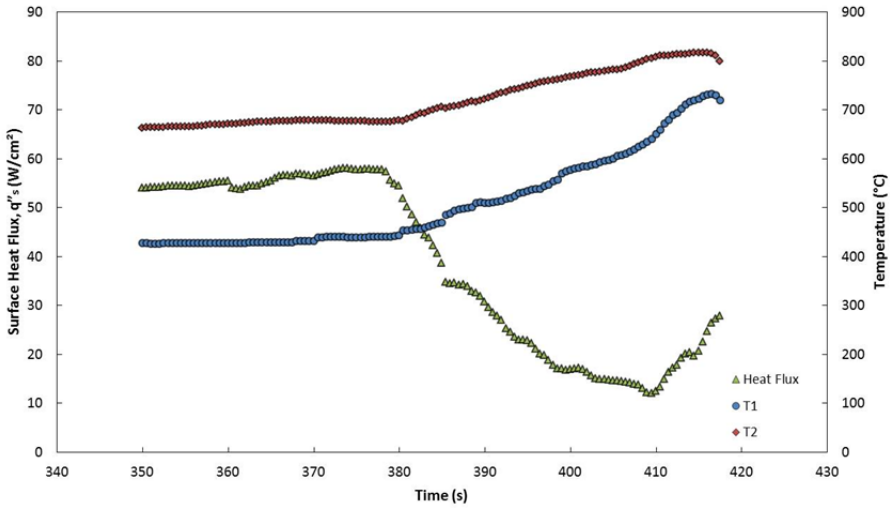

Figure 22. Heat flux and temperature vs. time response for one test illustrating the drop in heat flux and rise in temperature when CHF is reached.

Before determining the wall thermal resistance for each test, the measured heat flux is compared to the top sensor temperature to see how the heat flux responds to changes in temperature. Figure 23 illustrates the heat flux versus total temperature difference for each test. All four curves show a similar response up to about 320 °C. Afterward this point, tests 3 and 4 show the heat flux dropping significantly with increasing temperature while tests 5 and 6 show a small decrease in heat flux but then increases again and bounces around 500 kW/m² with increasing temperature. It appears that the boundary conditions are different, even though the conditions are the same for all four experiments, and it is unclear whether the torch flame creates a constant heat flux boundary condition, constant temperature boundary condition, or a combination of both. Regardless of whether the boundary condition created by the torch flame, CHF can be seen from all four responses and it is consistently around 500 kW/m². The variation of this value from the four tests shows that CHF is an unstable parameter.

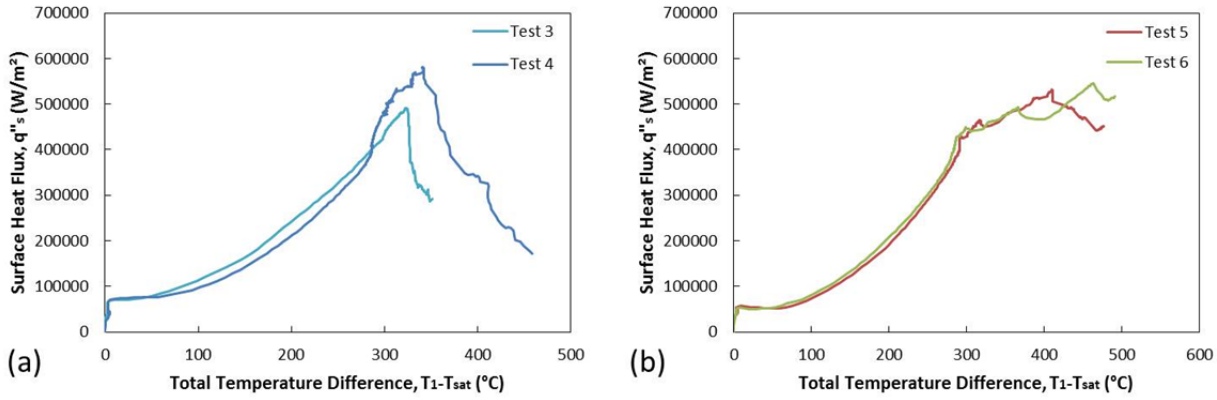

Figure 23. Heat flux vs. total temperature difference response curves from the oxy-acetylene tests: (a) Test3 and Test 4, (b) Test 5 and Test 6.

The total thermal resistance is observed to determine the range of data that can be used to calculate the wall thermal resistance and proportionality constant. The total thermal resistance has a decreasing trend between 100 °C and 300 °C, as illustrated in Figure 24. The least squares curve fit model is successfully able to determine wall thermal resistance and proportionality constant for all four tests, which are presented in Table 6. All four wall thermal resistance values are relatively consistent which show that the measurements are repeatable.

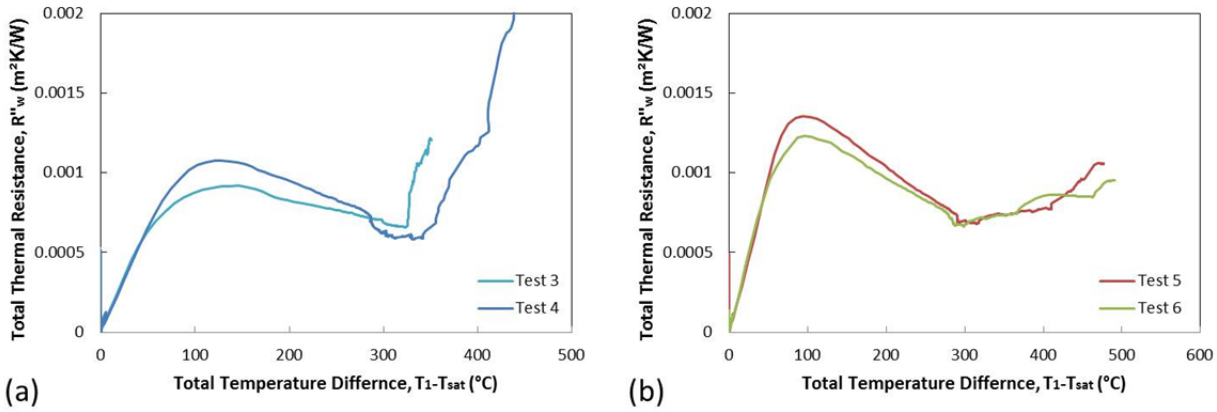

Figure 24. Total thermal resistance, Equation (28), vs. total temperature difference response curves from the oxy-acetylene tests: (a) Test3 and Test 4, (b) Test 5 and Test 6.

When the measured heat fluxes are plotted versus the calculated excess temperatures, illustrated in Figure 25, the responses are similar up to about 140 °C excess temperature for all four tests and then responses follow the same trend after that point that is described earlier. However, at this transition point the excess temperature is observed to decrease briefly with increasing heat flux. This behavior is an unexpected response and it is uncertain how this occurs physically. It may be possible that the contact resistances are increasing with increasing temperature. Based on the original data shown in Figure 23, around a total temperature difference of 280 °C the response shows an increase in heat flux with little to no temperature increase. All four data sets have this occurrence around the same temperature difference, and the responses deviate from the trend it follows up to that point. This point in the data shows an

anomaly in the boiling curves, but instead of the heat transfer coefficient beginning to decrease this inflection is due to a sudden increase in the heat transfer coefficient, as shown in Figure 26. Since the excess temperature is calculated using Equation (33) a sudden increase in the heat transfer coefficient, and thus the heat flux, with little to no change in the total temperature difference the excess temperature decreases in value.

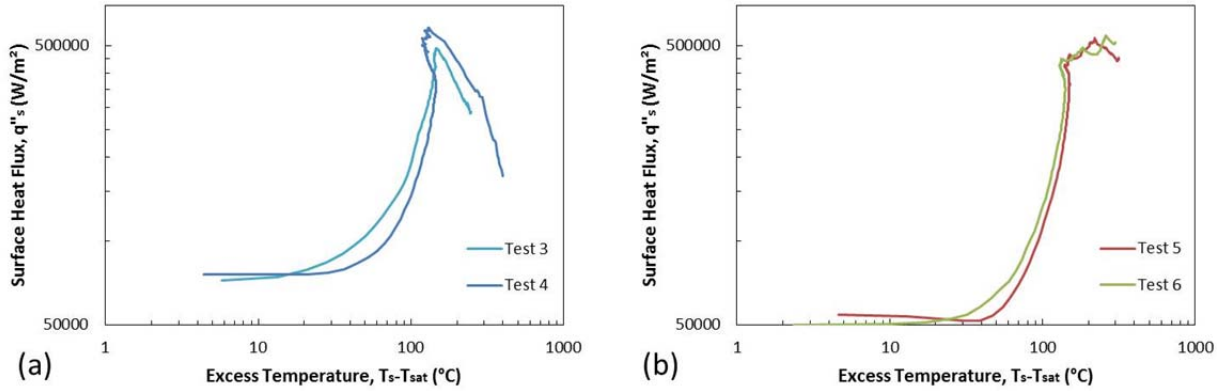

Figure 25. Experimental log-log boiling curves (measured heat flux vs. excess temperature) from the oxy-acetylene tests. The plots represent the boiling curves for: (a) Test3 and Test 4, (b) Test 5 and Test 6.

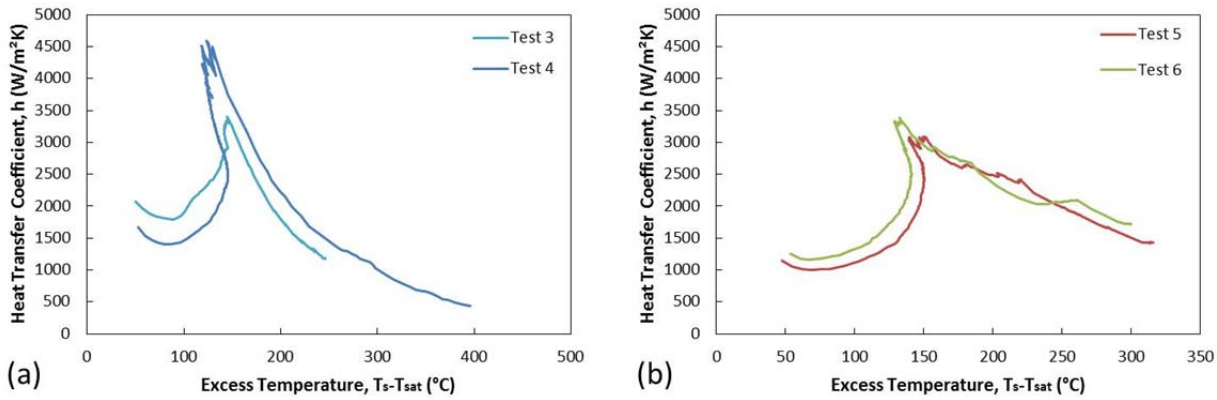

Figure 26. Heat transfer coefficient, Equation (34), vs. excess temperature response curves from the oxy-acetylene tests: (a) Test3 and Test 4, (b) Test 5 and Test 6.

The results show a consistent response up to an excess temperature of about 150 °C. The region below this excess temperature is classified as the nucleate boiling regime. After this point the heat flux is transitioning to film boiling, and as expected it is an unstable process as the response after the departure from nucleate boiling (DNB) is not as consistent between each test. CHF is evaluated at the DNB point. For tests 3 and 4 CHF is defined as the maximum heat flux achieved. For tests 5 and 6, the departure from nucleate boiling is determined by finding the excess temperature where the heat transfer coefficient begins to decrease. CHF is determined by averaging the heat flux values after DNB since it is unclear which point is considered CHF and the change of heat flux with increasing temperature is small. The values for CHF and corresponding excess temperature are presented in Table 6. Using the CHF values, an

equivalent CHF constant can also be calculated using Equation (3) which can be used for predicting CHF of similar systems.

Table 6. Calculated results determined from oxy-acetylene torch test data.

Parameters	Test 3 Values	Test 4 Values	Test 5 Values	Test 6 Values	Units
Critical Heat Flux, $q"_{max}$	491089	580852	482182	484817	W/m²
CHF Excess Temperature, $\Delta T_{e,max}$	144.90	129.51	151.47	132.69	°C
Wall Thermal Resistance, $R"_w$	0.000362	0.000365	0.000357	0.000370	m²K/W
Proportionality Constant, c	0.1524	0.1184	0.0959	0.1171	(W/m²)K³
Surface Coefficient, $C_{s,f}$	0.1242	0.1351	0.1450	0.1356	-
Equivalent CHF Constant, C	0.0598	0.0708	0.0588	0.0591	-

During the final test (Test 6) the heat flux level is cycled multiple times between nucleate boiling and transition to film to observe the response when the heat flux transitions across CHF. This is done by moving the torch closer to the wall until CHF is reached and removing the torch gradually until the heat flux transitioned back to nucleate boiling and this process is repeated a couple times. Figure 27 shows the response when the heat flux is moved back and forth across CHF. One observation from this result is that the heat flux around CHF is unsteady. However, typical responses can be seen when the heat flux transitions to film boiling. Definite CHF points occur approximately at 220 s and 388 s, where the heat flux drops and the temperature increases. The response at 348 s is questionable due to the drop in heat flux but the temperatures remain constant. Once CHF is observed at these points, the torch is removed gradually which causes the temperature to begin to drop. When the torch is removed, thus reducing the heat flux, the heat flux response is observed to drop initially as well but at some point during the temperature decrease the heat flux suddenly increases. This point in the response is identified as the point when the heat flux transitions back to nucleate boiling. The phenomenon appears to be consistent whenever the heat source is removed. Figure 28 is an extended curve from the heat flux vs. total temperature difference for Test 3. This phenomenon of the heat flux suddenly increasing in value at a certain point when the temperature is decreasing is clearly seen.

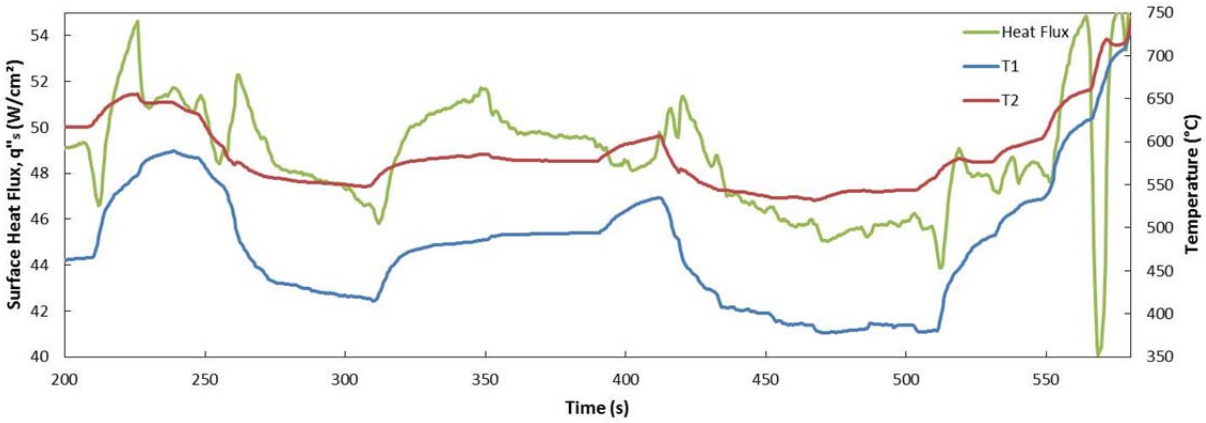

Figure 27. Heat flux and temperature response vs. time for Test 6, showing the response when the heat flux is adjusted back and forth across CHF.

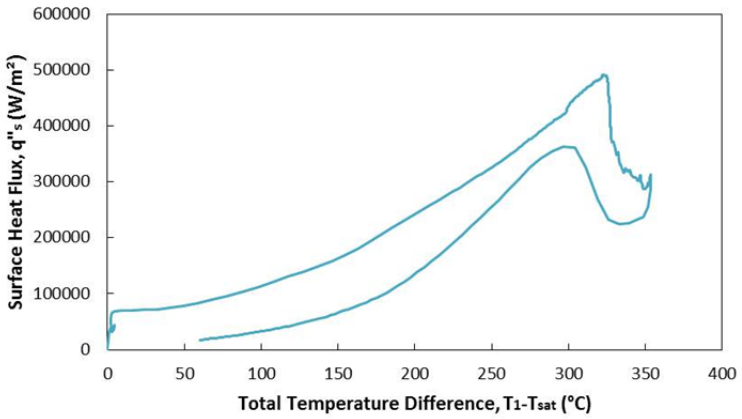

Figure 28. Extended heat flux vs. total temperature difference for Test 3 showing the increase of heat flux during the decrease of temperature, which is identified as the transition back to nucleate boiling.

6.3 Measurement Uncertainty Analysis. The quantities used to determine the heat flux contribute to the standard uncertainty of the heat flux measurements. The output voltage of the sensor, sensor sensitivity, average temperature, and thermal mass of the sensor are the only quantities that contribute to the uncertainty of the heat flux. The standard uncertainties for each of these quantities are determined using Type A and Type B methods, as described in Section 3.2.5.

The standard uncertainty for the output voltage is determined by calculating the sample standard deviation of the signal. For the electric heater test data, the data is averaged at each steady state step and the standard deviation is calculated for each range of steady state samples. For the torch test data, the standard uncertainty for each data point is estimated by calculating the percent standard deviation of the initial measured values, or when the heat flux is zero. The standard uncertainty for the sensitivity and thermal mass calculated in Section 3.2.5 is used here for determining the heat flux measurement uncertainty. The standard uncertainty for the average temperature is estimated based on the errors reported by the DAQ specifications and a value of 1.15 °C is used.

The standard uncertainty for the heat flux is calculated using the sequential perturbation technique [18] due to the complexity of Equation (11) since it contains the temperature derivative with respect to time. The expanded uncertainty is determined by multiplying the standard uncertainty by the coverage factor, κ, to get a 95% confidence interval for the measurement results. The coverage factor, as described in Section 3.2.5, is equal to the student's t-value for the corresponding degrees of freedom, where the effective degrees of freedom, N, is estimated using the Welch-Satterthwaite formula. The effective degrees of freedom for each test is estimated to be 50, which results in a coverage factor of 2.01. Both standard and extended uncertainties are calculated at each data point presented in this paper. The average extended uncertainty is estimated to be ±15.4% for the heat flux measurements.

The standard uncertainty for the wall thermal resistance, proportionality constant, and excess temperature are also estimated using the same procedure used for calculating the uncertainty for the heat flux measurements. The quantities that contribute to the uncertainty of these values are the heat flux, top sensor temperature T_1, and saturation temperature. The calculated standard uncertainty of the heat flux mentioned previously is used, and the standard uncertainties for both temperatures are presented in Table

7. The extended uncertainty for each value is calculated by multiplying the standard uncertainty by the coverage factor. Table 8 includes the coverage factor as well as the extended uncertainty for each value.

Table 7. Quantities used to calculate the standard uncertainties for the heat flux, wall thermal resistance, proportionality constant, and excess temperature.

Quantity	Standard Uncertainty, $u(x_i)$	Units
Sensitivity, S_0	(See Table 4)	-
Output Voltage, V_{out}	$V_{out} \times 0.0254$	μV
Thermal Mass, $\rho C_p \delta$	0.0614	J/cm²K
Average Temperature, T_{avg}	1.15	°C
Heat Flux, $q"_s$	$q"_s \times 0.077$	W/cm²
Top Sensor Temperature, T_1	1.15	°C
Saturation Temperature, T_{sat}	0.5	°C

Table 8. Extended uncertainties and coverage factors for measurement values.

Test #	$\kappa(q"_s)$	$U(q"_s)$, W/m²	$\kappa(R"_w)$	U$(R"_w)$, m²K/W	$\kappa(c)$	U(c), (W/m²)K³	$\kappa(\Delta T_e)$	U(ΔT_e), °C
1	2.01	$q"_s \times 0.159$	2.101	3.53×10^{-5}	2.101	1.643	2	$\Delta T_e \times 0.117$
2	2.01	$q"_s \times 0.155$	2.042	2.40×10^{-5}	2.042	0.561	2	$\Delta T_e \times 0.085$
3	2.01	$q"_s \times 0.156$	2	2.40×10^{-5}	2	0.069	2	$\Delta T_e \times 0.086$
4	2.01	$q"_s \times 0.150$	2	5.44×10^{-6}	2	0.065	2	$\Delta T_e \times 0.193$
5	2.01	$q"_s \times 0.151$	2	1.59×10^{-5}	2	0.058	2	$\Delta T_e \times 0.161$
6	2.01	$q"_s \times 0.151$	2	5.89×10^{-6}	2	0.066	2	$\Delta T_e \times 0.170$

7 Discussion

7.1 Application of Sensor for Boiling Heat Transfer. The use of heat flux sensors to get a direct measure of boiling heat fluxes is a technique currently not used for systems that employ boiling heat transfer as a means of transferring thermal energy. Results from these experiments show that a heat flux sensor is able to measure the heat flux up to CHF and survive the extreme environments. The same sensor is used for all the tests and is still functioning. While tests 1 and 2 did not reach CHF, they showed reliable results for the full range of data. Tests 3-6 achieved CHF based on the response and the determined value for CHF is fairly consistent considering that the transition to film boiling is not stable.

The heat flux sensor successfully measured values for CHF and beyond while surviving the extreme conditions that occur when operating in the film boiling regime. One reason for the system being able to survive these conditions is due to only heating a small area of the pipe and leaving the rest unheated. While the analytical model concluded that the one-dimensional assumption is valid, that assumption only applies during nucleate boiling. Once CHF is reached the area subjected to film boiling becomes insulated while the surrounding area is still subjected to nucleate boiling with the relatively thick pipe wall in these experiments. This causes the system to experience three-dimensional heat transfer effects which cause the energy to flow around the area subjected to film boiling. This allows the system to reach extreme

temperatures slowly because the system is still effectively cooled by the surrounding areas subjected to nucleate boiling.

7.2 Excess Temperature Measurements. One unusual observation in the results is the magnitude of the excess temperatures. For the electric heater test data, the maximum excess temperature is 63.24 °C without reaching CHF. Based on the temperature distribution from the analytical model, Figure 4, the excess temperature at CHF is estimated to be 20 °C. The difference is apparently due to the surface coefficients being different. For the analytical model, a value of 0.0132 is used for the surface coefficient which is the reported value for a stainless steel surface by Vachon [8]. The calculated surface coefficient of the experimental system is larger, around 0.050, which results in a higher excess temperature for the same heat flux. Since the heat flux applied by the electric heater is fairly uniform over the sensor area, as shown by the analytical model, the calculated surface coefficient is assumed correct for the test results using the electric heater. The difference in the surface constant may also be a factor of heating only a small area instead of the entire pipe.

For the torch test data, the average excess temperature for the determined CHF is about 140 °C. Compared to test 2, which has identical surface conditions as the torch tests, the excess temperature is much higher for the same heat flux. While not exact, the typical heat flux from an acetylene torch that is expected is around 100 W/cm² and only half of that is measured when CHF occurred. Also, the surface conditions for all four experiments with the torch are the same as test 2 from the electric heater test. The surface coefficients should be approximately the same, but the torch experiments have a surface coefficient of about 0.135 while the surface coefficient for test 2 is .056. Based on this, it seems that the measured heat fluxes with the torch are lower than the actual heat fluxes achieved. One reason this may be true is that the heat flux from the torch is not uniform, with it being the greatest at the center of the flame. The size of the torch tip is also small, with a 3/8 in. diameter which is slightly smaller than the length of the heat flux sensor. If the heat flux from the torch truly isn't uniform then it is impossible to have a uniform heat flux over the sensor area, and the sensor is measuring the average heat flux over the sensor area. Also, in order for the sensor to get the maximum output the flame needs to be centered exactly with the center of the sensor so that the heat flux distribution is symmetric. Due to the size of the flame compared to the sensor, small misalignments could result in skewed results as well. Assuming that the actual heat flux is higher than the measured heat flux, the actual excess temperatures will be lower due to the inverse relationship between excess temperature and heat flux in Equation (33).

7.3 Observation of CHF. Another observation from this study is that CHF is successfully observed, even if the measured value is inaccurate, and is occurs when the temperature begins to increase with no change or decreasing heat flux. Along with the observation of CHF, an anomaly in the response is observed in each test and it is a consistent indication that CHF is being approached. It occurs due to a sudden increase in the heat transfer coefficient with little to no change in temperature. This response change should be able to detect CHF without prior knowledge of when it occurs for a specific system. This observation validates one of the goals of this study. Further investigation in the validity of the heat flux response from the sensor should be performed to further confirm the findings of this study. Further investigation in using the heat flux output signal for feedback control should be performed for future research since the electric heaters were not able to provide enough heat flux to reach CHF, and the torch was not automatically controlled.

7.4 Future Improvements. The results from this study provide useful information for future improvements. The electric heaters are able to provide nearly uniform heat flux over the sensor area and the heat flux output is easily controlled but the heaters developed for this study did not survive. In order to reach CHF without developing a new heater, the acetylene torch was selected for the final experiment so that CHF could be observed. The acetylene torch is able to produce heat fluxes up to, or even beyond, CHF which is proved by the initial torch test with the plain pipe where the surface temperature got hot enough to turn red. However, as seen from the torch test results, the measured heat fluxes don't seem to be as high as they should be. An improvement for this system in providing accurate measurements is to develop a heat source that is able to provide heat fluxes in an excess of 100 W/cm^2 while having a large area relative to the sensor area. The failure of the electric heaters is due to poor thermal contact between the heating element and the pipe wall. The ceramic potting material and ceramic bonding material may not be the best material to use for providing a good thermal contact for the high temperatures experienced. Thermal expansion may also change the contact resistance during each experiment. During examinations of the heaters after use, it was found that the heater failed by one hot spot burning out which shows that the thermal contact was not uniform. While the developed heaters burned out before reaching CHF, it is desired to use an electric heater due to the control and constant heat flux boundary condition it provides. One method to improve performance of the existing heaters is to reduce the temperature difference across the pipe wall, which can be done by having a smaller wall thickness or using a different material. Another method is to improve the manufacture of the heater. Using techniques such as plasma spraying [17] a heating element can be sprayed onto any surface reducing the contact resistances between the heating element and surface. The heating element can be directly sprayed onto the inner diameter, but this would be difficult. The heating element may also be sprayed onto separate surface and then attached to or pressed against the inner diameter in the desired position. Another technique to manufacture a heater is to use a sheet of nichrome and laser etch the pattern to get the desired resistance, or use a thin sheet so the desired resistance is acquired without having to etch a pattern into it.

Improvements can also be done to the sensor itself. The sensor is also potted in the ceramic casting material which may have caused problems with thermal contact as well. Providing better thermal contact between the sensor and the surface will also reduce temperature differences. Developing a sensor that is deposited directly onto the surface may be a better way to provide good thermal contact, similar to the method of plasma spraying a heater onto a surface. This method may also allow the sensor to be smaller, which will allow the overall system to be more compact. For the purpose of experimenting, this will also allow the temperature differences to be smaller reducing the risk of the heating element burning out. Reducing the size of the sensor will also allow the sensor to be used in actual applications, such as fuel rods where the wall thicknesses are much smaller.

8 Conclusion

The heat flux sensor embedded in the wall of the pipe is able to successfully measure boiling heat fluxes up to CHF and beyond. The maximum heat flux measured with the electric heater is about 430 kW/m² with an excess temperature of 63 °C, but CHF is not achieved. By using an oxy-acetylene torch CHF is obtained and quantified by the heat flux sensor. CHF is determined to be about 510 kW/m² with an average excess temperature of 140 °C. All four tests with the torch show consistent data up to CHF. While it is believed that the actual heat fluxes for the torch tests are higher than the measured heat values, this study is not as concerned about accurately measuring CHF with the heat flux sensor but rather being able to observe that CHF has been obtained. The results presented in this study show a change in the response when CHF occurs. Each test also experiences a response change just before CHF and this phenomenon occurs approximately around the same temperature for each test. This response change is the result of a drastic increase in the heat transfer coefficient with little to no change in temperature and causes the heat flux trend to deviate from the cubic relationship with excess temperature for the nucleate boiling regime. This change in the response serves as an indication that CHF is near and validates that the heat flux sensor can be used for predicting CHF without prior knowledge of when it occurs.

References

[1] Nukiyama, S., "The Maximum and Minimum Values of the Heat Q Transmitted from Metal to Boiling Water Under Atmospheric Conditions," *Journal Japan Soc. Mech. Eng.,* **37**, p. 367-374, 1934 (Translation: *International Journal of Heat and Mass Transfer*, **9**, p. 1419-1433, 1966).

[2] Drew, T.B., and Mueller, A.C., "Boiling," *Trans. AIChE*, **33**, p. 449, 1937.

[3] Rohsenow, W.M., "A Method of Correlating Heat Transfer Data for Surface Boiling of Liquids," *Trans. ASME*, **74**, p. 969, 1952.

[4] Kutateladze, S.S., "On the Transition to Film Boiling Under Natural Convection," *Kotloturbostroenie*, **3**, p. 10, 1948.

[5] Zuber, N., *Trans. ASME*, **80**, p. 711, 1958.

[6] Yamagata, K., Kirano, F., Nishiwaka, K., and Matsuoka, H., "Nucleate Boiling of Water on the Horizontal Heating Surface," *Memoirs of the Faculty of Engineering of Kyushu University*, **15**, p. 98, 1955.

[7] Pioro, I.L., "Experimental Evaluation of Constants for the Rohsenow Pool Boiling Correlation," *International Journal of Heat and Mass Transfer*, **42**, p. 2003-2013, 1999.

[8] Vachon, R.I., Tanger, G.E., Davis, D.L., and Nix, G.H., "Pool Boiling on Polished and Chemically Etched Stainless Steel Surfaces," *Trans. ASME. Journal of Heat Transfer*, **90**, p. 231-238, 1968.

[9] Incropera, F.P., Dewitt, D.P., Bergman, T.L., and Lavine, A.S., Fundamentals of Heat and Mass Transfer, 6th ed., John Wiley & Sons, Hoboken, NJ, 2007.

[10] Lienhard, J.H., *A Heat Transfer Textbook*, 1st ed., Prentice-Hall, Englewood Cliffs, NJ, 1981.

[11] Kandlikar, S.G., "A Theoretical Model to Predict Pool Boiling CHF Incorporating Effects of Contact Angle and Orientation," *Trans. ASME. Journal of Heat Transfer,* **123**, p. 1071-1079, 2001.

[12] Kandlikar, S.G., and Steinke, M.E., "Contact Angle of Droplets During Spread and Recoil After Impinging on a Heated Surface," Trans IChemE, **79**, Part A, p. 491-498, 2001.

[13] Chang, Y.P., "An Analysis of the Critical Conditions and Burnout in Boiling Heat Transfer," USAEC Rep. TID-14004, Washington, DC, 1961.

[14] Gifford, A.R., Hubble, D.O., Pullins, C.A., Diller, T.E., and Huxtable, S.T., "Durable Heat Flux Sensor for Extreme Temperature and Heat Flux Enviroments," *Journal of Thermophysics and Heat Transfer*, **24**, No. 1, p.69-76, 2010.

[15] Hubble, D.O. and Diller, T.E., "A Hybrid Method for Measuring Heat Flux," *Journal of Heat Transfer*, **132**, 2010.

[16] Pullins, C.A. and Diller, T.E., "In situ High Temperature Heat Flux Sensor Calibration," *International Journal of Heat and Mass Transfer*, **53**, p. 3429-3438, 2010.

[17] Michels, D., Hadeler, J., and Lienhard, J.H., "High Heat Flux Resistance Heaters from VPS and HVOF Thermal Spraying," *Experimental Heat Transfer*, **11**, p. 341-359, 1998.

[18] R.S. Figliola, D.E. Beasley, Theory and Design for Mechanical Measurements, 4th ed., John Wiley and Sons, Inc., Hoboken, NJ, 2006. pp. 158–161.

[19] B.N. Taylor, C.E. Kuyatt, "Guidelines for evaluating and expressing the Uncertainty of NIST measurement results," *NIST Technical Note 1297*, National Institute of Standards and Technology, 1994.

[20]High Temperature Potting and Casting Materials, Aremco, 2013, Viewed May 1 2013, http://www.aremco.com/wp-content/uploads/2010/11/A04_13.pdf.
[21]High Temperature Ceramic & Graphite Adhesives, Aremco, 2013, Viewed May 1 2013, http://www.aremco.com/wp-content/uploads/2010/11/A02_13.pdf.
[22]Morgret, Daniel, M.S. Thesis (work in progress), Dept. of Electrical Engineering, 2013.

Appendix A: Numerical Model Setup

A two-dimensional, finite-difference model using the Gauss-Seidel method is created in MATLAB to model the temperature distribution in order to determine how close to one-dimensional heat transfer is achieved, under ideal conditions. The model divides the wall of the pipe into several nodes, uses a matrix coordinate system of (i, j), and calculates the temperature of each node based on the energy balance of the node. The diagram in Figure A 1 shows the layout for the model. The model it setup to work for any size matrix, with the number of rows and columns equal to *I* and *J*. The distances between each node in both directions are equal which allows the equations to be simplified and only one value for distance is needed. This distance varies depending on the number of nodes in each direction. The overall thickness is equal to the actual thickness of the pipe wall, which is equal to 0.218 inches, so the value for Δx and Δy is equal to the thickness divide by (*I*-1). The dotted lines represent the boundary for the energy balance equations for each node. The general energy equation for each node under steady conditions is shown as

$$\sum q_{cond} + q_{conv} + q_{in} = 0 \tag{A.1}$$

The q_{in} term is the heat input from the heater on the inner diameter of the pipe, which only covers about 1 in^2 surface area. Since the heat input is uniform over the area where it is applied, the heat input is written in terms of heat flux which is equal to the heater's power input divided by its surface area. This allows the same heat flux to be applied to each node regardless of the node's surface area. The conduction heat transfer term includes the heat transfer rates from neighboring nodes. The individual terms for the conduction heat transfer term is shown as

$$\sum q_{cond} = q_{(i+1,j)} + q_{(i-1,j)} + q_{(i,j+1)} + q_{(i,j-1)} \tag{A.2}$$

where a sample conduction heat transfer term is

$$q_{(i+1,j)} = \frac{k\,\Delta x\,w}{\Delta y}\left(T_{(i+1,j)} - T_{(i,j)}\right) \tag{A.3}$$

The width, w, is the length of the node in the third dimension and gets canceled since it is the same for all nodes, and the Δx and Δy terms change depending on the direction of heat transfer but are all equal anyway. The only difference occurs at the edges, shown in Figure A1, and the heat transfer along the edges includes a $\frac{1}{2}$ term due to the node area being half the size.The subscript for each heat transfer rate represents the coordinates of the node from which the thermal energy is transferred to node (i, j). The convective heat transfer term in Equation (A.1) in its general form is equal to

$$q_{conv} = hA_s(T_s - T_{sat}) \tag{A.4}$$

Equation (A.4) applies to both natural convection and nucleate boiling heat transfer, however depending on which condition the node is experiencing the heat transfer coefficient is found differently. By dividing the surface area on both sides in Equation (A.4) to get heat flux and setting it equal to Equation (1), the heat transfer coefficient for nucleate boiling is equal to

$$h_b = \mu_l\, h_{fg}\left[\frac{g(\rho_l - \rho_v)}{\sigma}\right]^{1/2}\left(\frac{C_{p,l}}{C_{s,f}\, h_{fg}\, Pr_l^n}\right)^3 (\Delta T_e)^2 \tag{A.5}$$

For natural convection, the heat transfer coefficient is found from the correlation for the average Nusselt number for natural convection, which is equal to

$$\overline{Nu}_L = \frac{\bar{h}L}{k} = K\, Ra_L^m \tag{A.6}$$

where the Rayleigh number equals

$$Ra_L = Gr_L Pr = \frac{g\beta(T_s - T_\infty)L^3}{\nu^2} Pr \tag{A.7}$$

For this system, T_∞ is equal to the saturation temperature of the water. Properties for the Rayleigh number are evaluated at the film temperature, which is the average of the surface temperature and the saturation temperature. The constant K and exponent m are equal to 0.59 and 0.25 respectively for a vertical plate. The characteristic length, L, is assumed to be equal to the unthreaded length of the tube which is about 4 inches (0.1 meters). For this model, the assumption is that nucleate boiling begins at an excess temperature of about 5 °C. The heat transfer coefficient derived from Equation (A.6) is estimated to be about 670.5 W/(m^{2}K) using the values from Table A2.

The heat flux input is adjusted so that the highest heat flux from the surface is equal to the estimated CHF at 1105.7 kW/m². For the case of zero natural convection the required heat flux input to reach CHF is 1149.686 kW/m². When natural convection is taken into consideration, the required heat flux input is 1149.688 kW/ m². The percent difference between the heat flux inputs including natural convection and assuming it to be zero is only 0.0001%. This means the assumption that natural convection heat transfer is nearly zero applies for this system. This is because the heat transfer coefficient for natural convection is proportional to the excess temperature to the one-fourth power, whereas the heat transfer coefficient for boiling is proportional to the excess temperature squared. In either case, only about 4% of the energy is lost to the surroundings. This means that nearly all the thermal energy is transferred to the water through boiling, and the one-dimensional assumption holds for this system.

Table A 1. Parameters used in the finite difference model.

Parameters	Values	Units
Saturation Temperature, T_{sat}	100	°C
Gravitational Acceleration, g	9.81	m/s²
Dynamic Viscosity, μ_l	2.79×10^{-4}	Pa·s
Liquid Density, ρ_l	957.85	kg/m³
Vapor Density, ρ_v	0.5956	kg/m³
Surface Tension, σ	0.0589	N/m
Enthalpy of Vaporization, h_{fg}	2257	kJ/kg
Specific Heat, $C_{p,l}$	4.217	kJ/(kg·K)
Prandtl Number, Pr_l	1.76	-
Thermal Conductivity, k	16	W/m·K
Surface Coefficient, $C_{s,f}$	0.0132	-
Fluid-Surface Exponent, n	1	-

Table A 2. Parameters used to estimate the heat transfer coefficient due to natural convection.

Parameters	Values	Units
Film Temperature, T_{film}	375	K
Gravitational Acceleration, g	9.81	m/s²
Kinematic Viscosity, ν_l	2.861×10^{-7}	m²/s
Characteristic Length, L	0.1	m
Thermal Expansion Coefficient, β	7.61×10^{-4}	1/K
Thermal Conductivity, k_l	0.681	W/m·K
Prandtl Number, Pr_l	1.7	-
Avg Temperature Difference, ΔT	5	K
Constant, K	0.59	-
Exponent, m	0.25	-

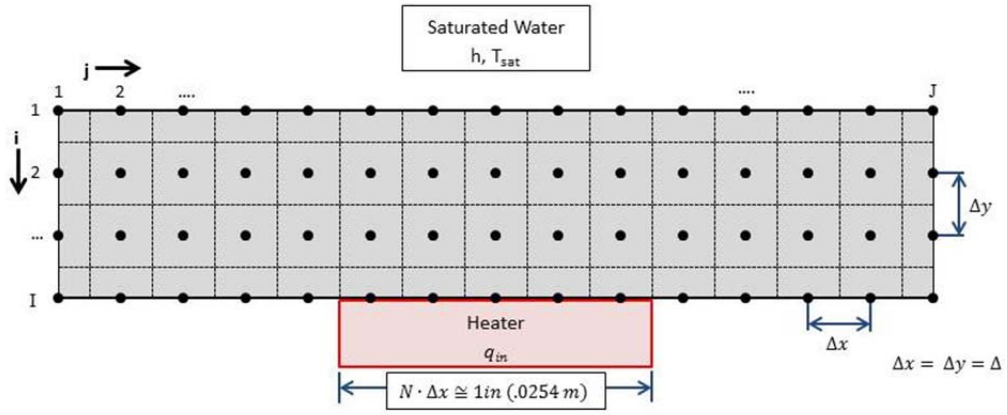

Figure A 1. Finite difference model diagram showing the layout of the nodes, including the coordinate system. The positions of the water and heater are shown for reference.

Appendix B: Least Squares Curve Fit Method

The general form for the least squares assumes that y is a linear function of K independent variables and a constant, and is shown as

$$y = a_0 + \sum_{k=1}^{K} a_k x_k \tag{B.1}$$

All measured data, with n number of observations, converts the general form into a matrix equation, written as

$$\begin{bmatrix} y_1 \\ y_2 \\ \vdots \\ y_n \end{bmatrix} = \begin{bmatrix} 1 & x_{1,1} & \cdots & x_{K,1} \\ 1 & x_{1,2} & \cdots & x_{K,2} \\ 1 & \vdots & \ddots & \vdots \\ 1 & x_{1,n} & \cdots & x_{K,n} \end{bmatrix} \begin{bmatrix} a_0 \\ a_1 \\ \vdots \\ a_K \end{bmatrix} \tag{B.2}$$

which can be rewritten as

$$\tilde{Y} = \tilde{X}\tilde{A} \tag{B.3}$$

where

$$\tilde{Y} = \begin{bmatrix} y_1 \\ y_2 \\ \vdots \\ y_n \end{bmatrix}, \qquad \tilde{X} = \begin{bmatrix} 1 & x_{1,1} & \cdots & x_{K,1} \\ 1 & x_{1,2} & \cdots & x_{K,2} \\ 1 & \vdots & \ddots & \vdots \\ 1 & x_{1,n} & \cdots & x_{K,n} \end{bmatrix}, \qquad \tilde{A} = \begin{bmatrix} a_0 \\ a_1 \\ \vdots \\ a_K \end{bmatrix} \tag{B.4}$$

The elements in $\tilde{Y}$ and $\tilde{X}$ are experimentally measured values and the elements in $\tilde{A}$ are unknown coefficients. Since experimental data normally does not exactly follow the equation in the form of Equation (B.1), there is no vector $\tilde{A}$ that will satisfy the equation. By using the sum of the squares of differences method between the elements of $\tilde{Y}$ and $\tilde{X}\tilde{A}$ a best fit curve can be found by setting the coefficient vector equal to

$$\tilde{A} = \left(\tilde{X}^T\tilde{X}\right)^{-1}\tilde{X}^T\tilde{Y} \tag{B.5}$$

Appendix C: Data Analysis Excel Code

To calculate the wall thermal resistance and proportionality constant, excel is used to apply the least squares curve fit model to the data. First a column of data for the total temperature difference, $T_1 - T_{sat}$, must be created. Similarly, a column for the surface heat flux data must be created. It is important that the surface heat flux is in units of W/m². A column of $q''^{1/3}_s$ is created in the column adjacent to the surface heat flux column (right side). Equation (B.5) used to solve for the wall thermal resistance and proportionality constant. The equivalent excel code for this equation is

=MMULT(MMULT(MINVERSE(MMULT(TRANSPOSE(D5:E33),D5:E33)),TRANSPOSE(D5:E33)), B5:B33)

Two rows and one column must be selected when typing in this equation. The D5:E33 range is the $\tilde{X}$ matrix, containing the heat flux and cube root of the heat flux, and the B5:B55 range is for the $\tilde{Y}$ array, which contains the temperature difference data. The ranges may be adjusted to match the actual locations of these arrays. Once the equation is inputted in excel, Ctrl+shift+enter is pressed to solve for the array. The first value, top row, will be the thermal resistance, and the second value, bottom row, will be equal to $(1/c)^{1/3}$.

Appendix D: New Slug Calorimeter Calibration Analysis

A new method for calibrating the thermal mass, $\rho C_p \delta$, of the HTHFS, used in Equation (9), is introduced which accounts for losses from the back side and losses due to re-radiation and convection. The energy balance for this method is shown in Figure 10b. Evaluating the energy balance, and by combining Equations (9) and (11) to solve for $q"_2$, gives

$$\rho C_p \delta \frac{dT_{avg}}{dt} = 2\left(q"_{abs} - q"_{conv} - q"_{rr} - q"_{diff}\right) = q"_{net} \tag{D.1}$$

The differential heat flux is the heat flux measured by the sensor itself based on the room temperature sensitivity from the differential calibration. Since the sensor outputs two heat flux signals they are averaged to give one value for the calibration.

The previous method found the thermal mass by inserting the heat flux term into the derivative with the temperature to give

$$\rho C_p \delta = \left(\frac{d}{dt}\left(\frac{T_{avg}}{q"_{net}}\right)\right)^{-1} \tag{D.2}$$

By doing so, the thermal mass can be found by finding the slope of $\frac{T_{avg}}{q"_{net}}$ vs. time and taking the inverse of the slope. A sample plot of this data is shown in Figure D1. Using this original method the thermal mass of the installed sensor is 0.933 J/cm²K.

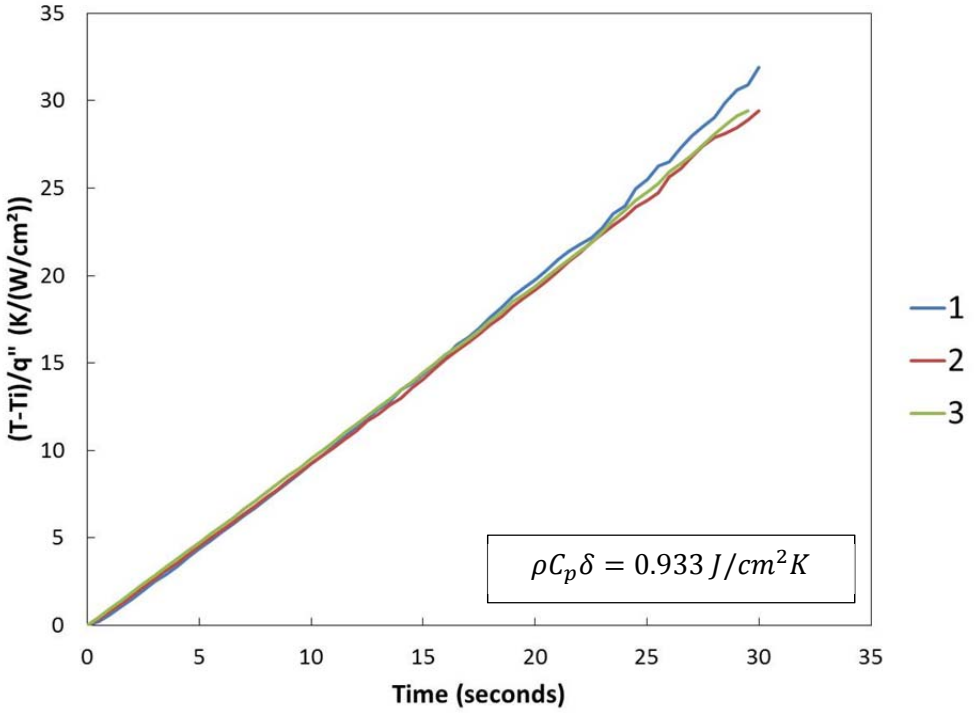

Figure D1. Temperature/heat flux vs. time plot. Original method for finding the thermal mass.

However, this original method only works if the heat flux term is constant. If the heat flux term is not constant then it cannot be placed in the derivative of the temperature. The heat flux term from the energy

balance in Equation (D.1) includes the re-radiation and differential heat flux terms which both increase with temperature. Evaluating Equation (D.2) gives

$$\rho C_p \delta = \left(\frac{d}{dt}\left(\frac{T_{avg}}{q"_{net}}\right)\right)^{-1} = \left(\frac{1}{q"_{net}}\frac{dT_{avg}}{dt} - \frac{T_{avg}}{(q"_{net})^2}\frac{dq"_{net}}{dt}\right)^{-1} \quad \text{(D.3)}$$

Since the heat flux is not constant, the second term ($\frac{dq"_{net}}{dt}$) does not equal zero and it is negative since the net heat flux is decreasing. As a result, the thermal mass from Equation (D.3) will be smaller than the true value. The true value of thermal mass is found by

$$\rho C_p \delta = \frac{q"_{net}}{\frac{dT_{avg}}{dt}} \quad \text{(D.4)}$$

By calculating this value for each data point collected, the thermal mass can be evaluated over the full data range and it should be constant. As seen in Figure D2, the thermal mass is relatively constant after about 2 seconds, and the thermal mass of the sensor can be evaluated by averaging the data after this time. The true value of the thermal mass for the installed sensor is 1.042 J/cm²K.

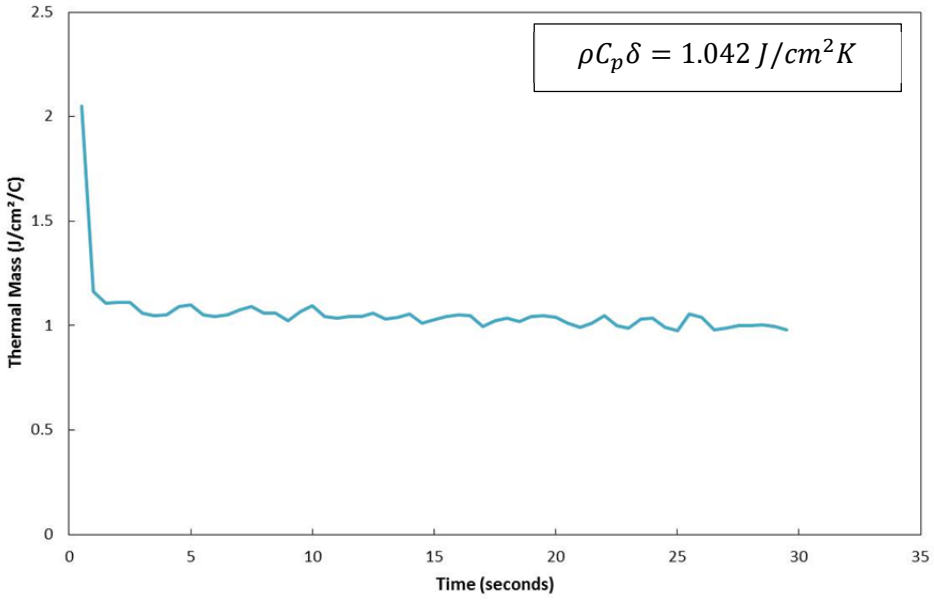

Figure D2. Sample thermal mass vs. time plot, showing the average thermal mass over the range of data.

Appendix E: Numerical Model Code

```
clc
clear all
close all

%% Constant values and parameters
Tsat = 100; % C
k = 16; % W/m*K, thermal conductivity of 304 stainless steel
g = 9.81; % m/s^2, acceleration of gravity
pf = 957.85; % kg/m^3, liquid density of saturated water
pg = .5956; % kg/m^3, vapor density of saturated water
s = .0589; % N/m, surface tension of water
Cp = 4217; % J/kg*K, specific heat of water
Cs = .0132; % mechanically polished, .0080 for ground and polished
n = 1;
hfg = 2257000; % J/kg, enthalpy of formation of sat. water
u = 279*10^(-6); % N*s/m^2, viscosity of water
Pr = 1.76; %prandtl number

% h = c*(Ts-Tsat)^2, qboil = c*(Ts - Tsat)^3
c = u*hfg*sqrt((g*(pf-pg))/s)*((Cp)/(Cs*hfg*Pr^n))^3;

%% Inputs
C = pi/24; % CHF constant
%pi/24 for horizontal cylinder, .098 for vertical surfaces

havg = 670.5; %W/m^2K

B = 60; %contact angle
phi = 90; %orientation angle

if havg == 670.5
    if C == pi/24
        q = 1149687.6; % Applied heat flux to I.D., W/m^2
    elseif C ==.098
        q = 861259.9;
    else
        C = ((1+cosd(B))/16)*((2/pi)+(pi/4)*(1+cosd(B))*cosd(phi))^.5;
        q = 657841.2;
    end
elseif havg == 0
    if C == pi/24
        q = 1149686.1; % Applied heat flux to I.D., W/m^2
    elseif C ==.098
        q = 861257.9;
    else
        C = ((1+cosd(B))/16)*((2/pi)+(pi/4)*(1+cosd(B))*cosd(phi))^.5;
        q = 657838.7;
    end
end

%% Matrices Setup
% Size of node matrix, row(I) vs. column(J)
I = 8;
```

```
J = 128;

% wall thickness = .218 in, 7*dx, 8 nodes
dx = (.218*.0254)/(I-1); % m

% Unthreaded length of pipe, must =~ 4 in
L = (dx*(J-1))/.0254; % inches

o = 49; p = 80;
Aq = zeros(1,J); %used to apply area where heat source is at the inside
surface
for i = o:1:p
    Aq(1,i) = 1;
end

A = 5000; %number of iterations

%Inital guess node matrix
T0 = 100*ones(I,J);
%matrices to be solved for
T = zeros(I,J);
h = zeros(1,J);
qboil = zeros(1,J);
dT = zeros(I,J);
Tp = zeros(A,J,I);

%% Node Temperature Solver: Gauss Seidel Method with damping for non-linear
equation

for a = 1:1:A

    %first column
    h(1,1) = havg;
    Bi1 = (h(1,1)*dx)/k;
       T(1,1) = (1/(2+Bi1))*(T0(2,1)+T0(1,2)+Bi1*Tsat);
       for i = 2:1:(I-1)
       T(i,1) = (1/2)*(T0(i,2)+.5*(T0(i-1,1)+T0(i+1,1)));
       end
       T(I,1) = (1/2)*(T0(I-1,1)+T0(I,2));

    %middle columns
   for j = 2:1:(J-1)
       if (T0(1,j)-Tsat)>=5
           h(1,j) = c*(T0(1,j) - Tsat)^2;
       else
           h(1,j) = havg;
       end
       Bi = (h(1,j)*dx)/k;

       T(1,j) = (Bi*Tsat+.5*(2*T0(2,j)+T(1,j-1)+T0(1,j+1)))/(2+Bi);
       for i = 2:1:(I-1)
       T(i,j) = (1/4)*(T0(i,j-1)+T0(i,j+1)+T0(i-1,j)+T0(i+1,j));
       end
       T(I,j) = (1/2)*(q*Aq(1,j)*dx/k + (1/2)*(2*T0(I-1,j)+T0(I,j-
1)+T0(I,j+1)));
```

```
   end

    %final column
    h(1,J) = havg;
    Bi2 = (h(1,J)*dx)/k;
       T(1,J) = (1/(2+Bi2))*(T0(2,J)+T0(1,J-1)+Bi2*Tsat);
       for i = 2:1:(I-1)
       T(i,J) = (1/2)*(T0(i,J-1)+.5*(T0(i-1,J)+T0(i+1,J)));
       end
       T(I,J) = (1/2)*(T0(I-1,J)+T0(I,J-1));

    %equation adjustment for iteration
   for j = 1:1:J
       for i = 1:1:I
           T0(i,j) = T0(i,j)+(T(i,j)-T0(i,j))/4;
       end
   end

%    for j = 1:1:J %used for iteration plots
%        for i = 1:1:I
%         Tp(a,j,i) = T(i,j);
%        end
%    end

end

% % Iteration Plots for each node to check for convergence
%     figure(3)
%     subplot(4,1,1),plot((1:1:A),Tp(:,40,1))
%     subplot(4,1,2),plot((1:1:A),Tp(:,40,3))
%     subplot(4,1,3),plot((1:1:A),Tp(:,40,5))
%     subplot(4,1,4),plot((1:1:A),Tp(:,40,8))

%% Delta T matrix: temperature difference between the last and next-to-last
iteration
for j = 1:1:J
    for i = 1:1:I
        dT(i,j) = (T(i,j)-T0(i,j));
    end
end

%% Heat transfer coefficient and heat flux distribution plots at surface

for j = 1:1:J
    qboil(1,j) = h(1,j)*(T(1,j)-Tsat);
end

%sensor location
xs1 = ((J-1)*dx*.5)-(.38*.0254*.5);
xs2 = ((J-1)*dx*.5)+(.38*.0254*.5);

x = 0:dx:(J-1)*dx;
figure(1)
subplot(2,1,1),plot(x,h,'b',[xs1 xs1],[0 60000],'k',[xs2 xs2],[0 60000],'k')
xlabel('Axial Position (m)','fontsize',15)
```

```
ylabel('Heat Transfer Coefficient (W/m^2K)','fontsize',15)
% title('Heat Transfer Coefficient Distribution','fontsize',15)
set(gca,'fontsize',15)
xlim([0 .1005])
subplot(2,1,2),plot(x,qboil,'b',[xs1 xs1],[0 12e5],'k',[xs2 xs2],[0
12e5],'k')
% title('Surface Heat Flux Distribution','fontsize',15)
xlabel('Axial Position (m)','fontsize',15)
ylabel('Heat Flux (W/m^2)','fontsize',15)
set(gca,'fontsize',15)
xlim([0 .1005])

%% Temperature Distribution plots

figure(2)
subplot(2,1,1),plot(x,T(1,:),'b',[xs1 xs1],[100 125],'k',[xs2 xs2],[100
125],'k')
xlabel('Axial Position (m)','fontsize',15)
ylabel('Temperature (^{\circ}C)','fontsize',15)
set(gca,'fontsize',15)
xlim([0 .1005])
subplot(2,1,2),plot(x,T(I,:),'b',[xs1 xs1],[100 600],'k',[xs2 xs2],[100
600],'k')
xlabel('Axial Position (m)','fontsize',15)
ylabel('Temperature (^{\circ}C)','fontsize',15)
set(gca,'fontsize',15)
xlim([0 .1005])

Tsmax = max(T(1,:));
Timax = max(T(I,:));
deltaTw = Timax - Tsmax;
%% Critical Heat Flux

qcrit = C*hfg*pg*((s*g*(pf-pg))/pg^2)^(1/4) %W/m^2
K = 0;
for j = 1:J
    if Aq(1,j) == 1
        K = K+1;
    end
end
[qboilmax,nodemax] = max(qboil)
dq = qcrit-qboilmax

%% Power Requirement
qi = q * (K*dx)^2 % power required to heat the surface, W

pd = (q-qcrit)/(mean([q qcrit]))*100;
pe = (q-qcrit)/qcrit*100;

%% Uniformitiy and 1-D Analysis

for i = 58:1:71
    qu(1,i-58+1) = qboil(i);
    xu(1,i-58+1) = x(i);
end
```

```
X = x(p)-x(o-1);
qout = trapz(xu,qu)*X;
qoutt = trapz(x,qboil)*x(I);

qavg = mean(qu); %average heat flux for sensor area
```

Appendix F: Sensitivity Calibration/Uncertainty Code

```
%% Sensitivity Calibration file
%  For differential heat flux

close all; clear all; clc;

eg=0.94; %sensor surface emissivity (coated with Zynolite, no high temp.
cure)


%% load data file(s)
filepath1='\\vtcadserv3.cadlab.vt.edu\Users\jthom07\My Documents\Research\DNB
Sensor\Data\final_recal.lvm';
% filepath1='C:\Users\Jordan\Documents\Class-Research\Research\DNB
Sensor\Data\final_recal.lvm'; %make sure filepath is correct
fid=fopen(filepath1);
for j=1:23
    erase=fgetl(fid);
end
num_cols=5; %number of columns in raw data file
a=fscanf(fid, '%f',[num_cols, inf]); A=a'; fclose(fid);
time=A(:,1); tc1=A(:,2); tc2=A(:,3); hfv1=A(:,4); hfv2=A(:,5);

%remove sensor voltage bias
v1_offset=mean(hfv1(1:90)); hfv1=hfv1-v1_offset;
v2_offset=mean(hfv2(1:90)); hfv2=hfv2-v2_offset;

%individual test conditions
ss=[395 570 740 870 1000 1120 1310]; %start time for each steady-state heat
flux event

v=[40.18 50.43 60.42 70.32 80.68 90.07 119.91]; %variac voltage at steady
state (read with true RMS multimeter)

%% steady state calculations
num_samples=30; %average steady-state data over 30 seconds (sampling rate = 1
Hz)
for i=1:length(ss)
    TC1(i)=mean(tc1(ss(i)-num_samples:ss(i)));
    TC2(i)=mean(tc2(ss(i)-num_samples:ss(i)));
    V1(i)=mean(hfv1(ss(i)-num_samples:ss(i)));
    V2(i)=mean(hfv2(ss(i)-num_samples:ss(i)));
end

%% data processing
Tavg_1=(TC1+TC2)./2;

%heat flux
p=[ 1.7772718e-10, -0.00000051537166, 0.00018497218, 0.0022517471, 0];
%polynomial coefficients for voltage (VAC RMS) to incident radiation heat
flux conversion
%re-calibrate periodically
%sensor face 1.25 inches from edge of reflector
```

```
HFabs=eg.*polyval(p,v); %absorbed heat flux, W/cm^2
S1=V1*10^6./HFabs %HTHFS sensitivity, microV/W/cm^2
S2=V2*10^6./HFabs

S1a = mean(S1)
S2a = mean(S2)

%% plots

%sensor voltage vs time
figure; hold on; box on;
plot(time,hfv1, 'b-',time,hfv2,'r--','linewidth',2);
legend('HFV1','HFV2')
xlabel('Time, {\itt}
(s)','FontSize',10,'FontName','Helvetica','FontWeight','bold')
ylabel('HTHFS Voltage, {\itV}_{t}
(V)','FontSize',10,'FontName','Helvetica','FontWeight','bold')
hold off

figure (2)
subplot(2,2,1),plot(HFabs,V1*1000000,'-
bs','linewidth',2,'markersize',5,'markerfacecolor','r')
title('Signal Output vs. Heat Flux, HF1 (Alumel)')
xlabel('Net Absorbed Heat Flux, W/cm^2')
ylabel('Voltage Output, {\mu}V')
axis([0 2.5 0 800])
grid on
subplot(2,2,2),plot(HFabs,S1,'bs','markerfacecolor','r','markersize', 10)
title('Sensitivity Plot, HF1 (Alumel)')
xlabel('Net Absorbed Heat Flux, W/cm^2')
ylabel('Sensitivity, {\mu}V/ (W/cm^2)')
axis([0 2.5 330 360])
subplot(2,2,3),plot(HFabs,V2*1000000,'-
bs','linewidth',2,'markersize',5,'markerfacecolor','r')
title('Signal Output vs. Heat Flux, HF2 (Chromel)')
xlabel('Net Absorbed Heat Flux, W/cm^2')
ylabel('Voltage Output, {\mu}V')
axis([0 2.5 0 800])
grid on
subplot(2,2,4),plot(HFabs,S2,'bs','markerfacecolor','r','markersize', 10)
title('Sensitivity Plot, HF2 (Chromel)')
xlabel('Net Absorbed Heat Flux, W/cm^2')
ylabel('Sensitivity, {\mu}V/ (W/cm^2)')
axis([0 2.5 260 290])

%% uncertainty

v1 = V1*10^6; v2 = V2*10^6; HFV1 = hfv1*10^6; HFV2 = hfv2*10^6;
uq2 = [0.005316029 0.007644595 0.010503097 0.013759447 0.016511742 0.02041971
0.032671839];
vq2 = [1.5132875 1.23816534 1.207211715 1.21597356 1.290880396 1.200635953
1.261501382 1.237835267 1.279394064 1.237837301];

ue = .05/sqrt(3); uV = .2/sqrt(3);
```

```
for i=1:length(ss)
    u1r(i) = std(HFV1(ss(i)-num_samples:ss(i)));
    u2r(i) = std(HFV2(ss(i)-num_samples:ss(i)));

    u1sys(i) =
sqrt((.031915*v1(i))^2+(.014388*v1(i))^2+(.039007*v1(i))^2+(.035971*v1(i))^2)
;
    u2sys(i) =
sqrt((.02682*v2(i))^2+(.01983*v2(i))^2+(.049808*v2(i))^2+(.031161*v2(i))^2);

    u1v(i) = sqrt((u1sys(i))^2+(u1r(i))^2);
    u2v(i) = sqrt((u2sys(i))^2+(u2r(i))^2);

    dqde = polyval(p,v(i));
    dqdV = (4*p(1)*v(i)^3)+(3*p(2)*v(i)^2)+(2*p(3)*v(i))+p(4);
    uq1(i) = sqrt((dqde*ue)^2+(dqdV*uV)^2);
    vq1(i) = ((uq1(i))^4)/sum([((dqde*ue)^4)/1000 ((dqdV*uV)^4)/1000]);

    uq(i) = sqrt((uq1(i))^2+(uq2(i))^2);
    vq(i) = vq1(i)+vq2(i);

    us1(i) = sqrt(((1/HFabs(i))*u1v(i))^2+((v1(i)/(HFabs(i))^2)*uq(i))^2);
    us2(i) = sqrt(((1/HFabs(i))*u2v(i))^2+((v2(i)/(HFabs(i))^2)*uq(i))^2);

    ve1(i) = ((us1(i))^4)/sum([(((1/HFabs(i))*u1v(i))^4)/29
(((v1(i)/(HFabs(i))^2)*uq(i))^4)/vq(i)]);
    ve2(i) = ((us2(i))^4)/sum([(((1/HFabs(i))*u2v(i))^4)/29
(((v2(i)/(HFabs(i))^2)*uq(i))^4)/vq(i)]);
end

us1a = mean(us1);
us2a = mean(us2);

ve = mean([mean(ve1) mean(ve2)]);
```